Conformational dynamics of a nicotinic receptor neurotransmitter site

Mrityunjay Singh[1], Dinesh C. Indurthi[2], Lovika Mittal[1], Anthony Auerbach[2], and Shailendra Asthana[1].

[1]Computational Biophysics and CADD Group, Computational and Mathematical Biology Center, Translational Health Science and Technology Institute, NCR Biotech Science Cluster, Faridabad 121001, India.

[2]Department of Physiology and Biophysics, University at Buffalo, State University of New York, Buffalo, United States.

Corresponding Authors

Shailendra Asthana: sasthana@thsti.res.in

Anthony Auerbach: Anthony.auerbach@gmail.com

Dinesh C. Indurthi: dinesh.indurthi@gmail.com

Key words: acetylcholine, allostery, agonist, molecular dynamics, ion channel

Abstract

Agonists increase receptor activity by providing net-favorable binding energy to active versus resting conformations of their target sites. We used molecular dynamics (MD) simulations to explore dynamics of the low-to-high affinity conformational change (L→H) at the *Torpedo* α–δ nicotinic acetylcholine receptor neurotransmitter site, using 4 agonists. Alternative conformations were identified in trajectories generated from a single starting structure by matching approximate binding energies calculated *in silico* with exact values measured experimentally *in vitro*. In all simulations, the L→H transition started with a rotation of the agonist about its cationic center ('flip'), followed by a staged downward displacement of loop C ('flop') and the formation of a compact, hydrophobic and stable high-affinity pocket ('fix'). Agonist rotation and a transient intermediate state are only in simulations but can be confirmed or refuted, for example by time-resolved structures.

35 **Introduction**

36 Adult vertebrate nicotinic acetylcholine receptors (AChRs) are allosteric proteins that mediate
37 synaptic transmission between motor neurons and skeletal muscle fibers. These pentameric ligand-
38 gated ion channels are composed of four different subunits (2 α1, β1, δ, ε) arranged symmetrically
39 around a central ion-conducting pore (Rahman et al., 2020; Unwin, 1993). Interactions between the
40 neurotransmitter acetylcholine (ACh) and orthosteric sites in the extracellular domain (ECD) increase
41 the probability of a global change in protein conformation that opens a distant (~60 Å) allosteric site (a
42 'gate') in the transmembrane domain (TMD), allowing cations to cross the membrane. In AChRs the
43 ligand-protein interactions occur sequentially in reactions called 'touch' (initial contact), 'catch' (agonist
44 recognition) and 'hold' (receptor animation) (Auerbach, 2024; Jadey & Auerbach, 2012). Here, we use
45 MD simulations to investigate restructuring of a neurotransmitter site in hold.

46 The. neurotransmitter sites switch from low- to high-affinity at the start of the global gating
47 isomerization, and the gate switches from closed to open at the end the isomerization (C→O)
48 (Grosman et al., 2000; Purohit et al., 2013). We represent the overall gating conformational change of
49 the receptor as $C_L \rightleftarrows O_H$, with capital letters indicating the functional status of the gate and subscripts
50 indicating the functional status of the neurotransmitter sites.

51 Receptors change conformation (turn on and off) spontaneously, influenced only by
52 temperature. In AChRs without agonists, a large energy barrier separates C_L from O_H so the probability
53 of having the open-gate shape (P_O) small (~10^{-6}) and the baseline current is negligible (Jackson, 1986;
54 Nayak et al., 2012; Purohit & Auerbach, 2009). The higher affinity of O_H compared to C_L indicates that
55 agonists stabilize this state preferentially, to increase P_O and membrane current. Importantly, agonists
56 also stabilize the gating transition state (reduce the separating barrier) to nearly the same extent as the

57 end states, so the agonist-induced increase in P_O is caused almost exclusively by an increase in the
58 channel-opening rate constant. Consequently, neurotransmitters turn on AChRs rapidly to generate a
59 fast-rising synaptic impulse.

60 Agonists are characterized by affinity, efficacy and efficiency. Each orthosteric site has two
61 affinities (agonist binding free energies), weak to L and strong to H. Their difference, H minus L (ΔG_H-
62 ΔG_L), is the energy source that drives the otherwise unfavorable protein isomerization. This difference,
63 plus the agonist-independent free energy of unliganded gating, determines the maximum of the dose-
64 response curve (efficacy). The binding energy difference is the *amount* of free energy delivered to the
65 gating apparatus at each orthosteric site.

66 A related, but distinct, agonist property is efficiency that, in contrast to efficacy, depends on the
67 H/L binding free energy ratio, ($1-\Delta G_L/\Delta G_H$) (Nayak et al., 2019). This ratio determines the *fraction* of
68 binding free energy converted into local movements that stabilize the gating transition state and,
69 hence, animate the protein. In a dose-response curve, efficiency is manifest as the correlation
70 between the maximum response and EC_{50} (Indurthi & Auerbach, 2023). Like affinity and efficacy,
71 efficiency is a universal agonist attribute (Auerbach, 2024).

72 The salient energy changes at the orthosteric sites of adult-type muscle AChRs have been
73 estimated experimentally by using electrophysiology (Figure 1A). These receptors have 2
74 approximately equal and independent neurotransmitter sites (Nayak & Auerbach, 2017). The total free
75 energy change in the L→H transition for two neurotransmitters (-10.2 kcal/mol), added to the
76 unfavorable unliganded isomerization free energy change (+8.3 kcal/mol at -100 mV), generates a
77 favorable free energy change of gating (-1.9 kcal/mol) (Nayak et al., 2012). ΔG is proportional to the
78 logarithm of the corresponding equilibrium constant by -RT, where R is the gas constant and T the

79 absolute temperature (RT equals 0.59 at 23 ^{o}C). Accordingly, the two independent L→H
80 rearrangements add to increase the gating equilibrium constant by a factor of 5680[2], to increase P_O
81 from 7.4x~10^{-7} to 0.96 (Nayak et al., 2012). Likewise, the L→H rearrangements increase the opening
82 rate constant by almost the same factor, from ~0.001 s^{-1} to ~50,000 s^{-1}. The result is a nearly perfect
83 synaptic current that rises rapidly from almost zero to almost maximum (Jackson, 1989).

84 Agonist free energy changes in catch and hold determine affinity and efficacy. Our goal was to
85 associate the $\Delta G_L \rightarrow \Delta G_H$ change in binding free energy associated with hold with local structural
86 rearrangements at an AChR neurotransmitter site. MD simulations were used to explore
87 conformational changes in the L→H transition at the $\alpha-\delta$ neurotransmitter site of the *Torpedo* AChR
88 (6UVW; (Rahman et al., 2020)). In brief, for 4 agonists L and H conformations were identified in the
89 simulations, and binding free energies calculated approximately *in silico* matched those measured
90 accurately (by using electrophysiology) *in vitro*. In L→H, 3 rearrangements were prominent for all
91 agonists: 1) a rotation of the ligand abouts its cationic center ('flip'), 2) a downward displacement of
92 loop C ('flop'), and 3) compaction, dehydration and stabilization of the pocket ('fix'). Also, for all
93 agonists a brief intermediate state connected the initial L and final H conformations. These results
94 suggest that movement of the agonist may start the conformational change that turns on the receptor.

95

96 **Results**

97 <u>*Hold.*</u> Traditionally, receptor activation is divided into distinct steps called 'binding' (formation of a
98 ligand-protein complex) and 'gating' (receptor isomerization) (Figure 1). Here, we are concerned with
99 their connection in the form of structural changes at a neurotransmitter site.

100 In AChRs, both binding and gating are aggregate processes (Figure 1). First, the agonist (A)
101 diffuses to and contacts the resting target (touch), forming an encounter complex, A-C. This step is
102 approximately the same for small agonists. Then, a local protein rearrangement (catch) establishes the
103 low affinity complex, AC_L. The expanded binding reaction scheme is $A+C \rightleftarrows A\text{-}C \rightleftarrows AC_L$ (Jadey & Auerbach,
104 2012). Gating involves sequential structural changes in receptor domains (Gupta et al., 2017; Purohit et
105 al., 2013). First, each neurotransmitter site undergoes another local rearrangement (hold) that
106 establishes the high-affinity complex (AC_H), after which other domains restructure without a further
107 change in agonist affinity, eventually opening the gate (isomerize). The expanded gating reaction
108 scheme is $AC_L \rightleftarrows AC_H \rightleftarrows \ldots \rightleftarrows AO_H$ (Figure 1B). AC_L is both the end state of 'binding' and the start state of
109 'gating'. Our interest here is the structural changes in the hold transition that links binding with gating,
110 $AC_L \rightleftarrows AC_H$.

111 In AChRs, rearrangements that change agonist energy in catch (ΔG_L) and in hold ($\Delta G_H - \Delta G_L$) are
112 localized to the two orthosteric sites. Energy changes associated with the other events in the
113 activation sequence, namely the chemical potential associated with touch (Phillips, 2020) and
114 downstream domain restructurings in the rest of the isomerization (Gupta et al., 2017) are
115 approximately agonist-independent and not relevant to setting relative affinity, efficacy or efficiency.
116 Although there are proposals and reports suggesting that protein-protein interactions at the ECD-TMD
117 interface influence agonist binding energy, these are either unsupported (Cymes & Grosman, 2021;
118 Gupta et al., 2017; Nayak et al., 2012) or in error (Purohit et al., 2015). So far, only mutations at
119 neurotransmitter sites have been shown to influence agonist binding energy.

The agonist's local energy changes at each orthosteric site in catch and in hold determine relative affinities (ΔG_L and ΔG_H), efficacy ($\Delta G_H - \Delta G_L$) and efficiency ($1-\Delta G_L/\Delta G_H$). In AChRs, ΔG_L and ΔG_H have been measured experimentally by using electrophysiology for 23 agonists and 53 neurotransmitter site mutations (Indurthi & Auerbach, 2023), and these values serve as a basis for identifying L and H structures in the MD simulations.

Apo, resting-C (with a bound toxin), and high-affinity desensitized AChR structures have been solved by using cryo-EM (Rahman et al., 2022; Rahman et al., 2020; Zarkadas et al., 2022). Desensitized (D) AChRs have a similar, perhaps identical, high affinity as O_H (Auerbach, 2020; Nayak & Auerbach, 2017). Below, we report the results of MD simulations regarding the conformational dynamics that connect the end states of the hold rearrangement, $AC_L \rightarrow AC_H$ (Figure 1B, bottom), the event that triggers the isomerization that eventually opens the gate. Although neither is these states have been captured as a stable structure, the results suggest that they can be identified in MD simulations.

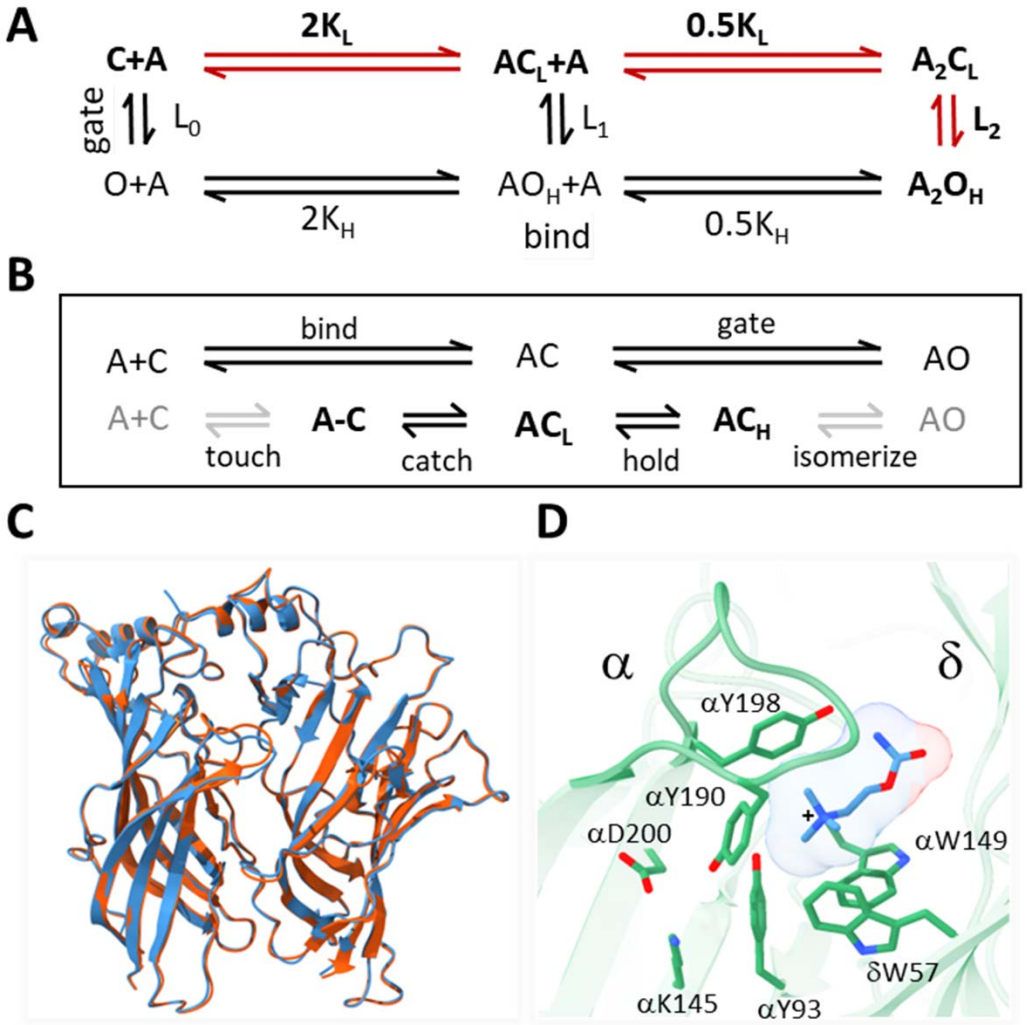

Figure 1: AChR activation. *A. Traditional scheme.* Vertical is 'gating' and horizontal is 'binding'; red, main physiological pathway. The isomerization between closed-channel/low-affinity (C_L) and open-channel/high-affinity (O_H) conformations occurs with or without agonists (equilibrium constant L_n; n, number of bound ligands), and is spontaneous (depends only on temperature) and global (on a ~µs time scale). Agonists (A) bind weakly to C_L (equilibrium association constant K_L, free energy change ΔG_L) and strongly to O_H (K_H, ΔG_H). The 2 orthosteric sites of adult AChRs are approximately equivalent and independent and there is no significant external energy, so $L_2/L_0 = (K_H/K_L)^2$ (Nayak & Auerbach, 2017). B. Expansions of binding (top, ends with catch) and gating (bottom, starts with hold). The agonist diffuses to and contact the target ('touch') to form an encounter complex (A-C); a local 'catch' rearrangement establishes the low affinity complex (AC_L); a local 'hold' rearrangement establishes the high affinity complex (AC_H); the remaining protein domain 'isomerize' without a further change in affinity to generate a conducting channel (AO_H). Gray arrows, steps that incur the same energy change for all agonists used in this study; black arrows, agonist-dependent free energy changes occur in catch (ΔG_L) and in hold (ΔG_H-ΔG_L). C. α-δ subunit extracellular domains; red, after toxin removal (6UWZ.pdb) and blue, apo (7QKO.pdb). There are no major deviations (C_α RMSD = 0.3 Å). D. Closeup of the desensitized *Torpedo* α-δ subunit neurotransmitter site occupied by carbamylcholine (CCh, blue) (7QL6.pdb; (Zarkadas et al., 2022)). In this is H conformation, 3 aromatic groups in the α subunit (149-190-198) surround the agonist's cationic center (+) together provide most of the ACh binding energy (Purohit et al., 2014); the agonist's tail points away from the α subunit (*trans* orientation).

152 *Docking.* We began by removing α-bungarotoxin from the 2.69 Å resolution structure of resting-C
153 (6UWZ; (Rahman et al., 2020) (Figure 1C) and docking agonists into the now-empty pocket. The
154 docking simulations had strong binding scores ranging from -5.82 to -9.18 kcal/mol (Figure 2A),
155 suggesting that the interactions were stable. However, unlike the agonist orientation apparent in cryo-
156 EM structures of D_H (Noviello et al., 2021; Rahman et al., 2022; Rahman et al., 2020; Walsh et al., 2018;
157 Zarkadas et al., 2022) (Figure 1D), the docked agonist's tail pointed towards (*cis*) rather than away
158 (t*rans*) from the α subunit (Figure 2B, top). This was a consistent result that pertained to the 3 top
159 docking poses for all 4 ligands.

160 Because the *cis* orientation was not observed in any cryo-EM structure, we examined the top
161 200 docking scores for CCh. All poses were *cis*, with the tail pointing towards the α subunit and away
162 from the main cluster of aromatic side chains. Apparently, in the unliganded 6UWZ and 7QKO
163 structures (Figure 1C), the *trans* orientation observed in 7QL6 is unfavored. These results suggested
164 that the agonist orientations in the end states are *cis* in AC_L versus *trans* in AC_H.

165

166

167

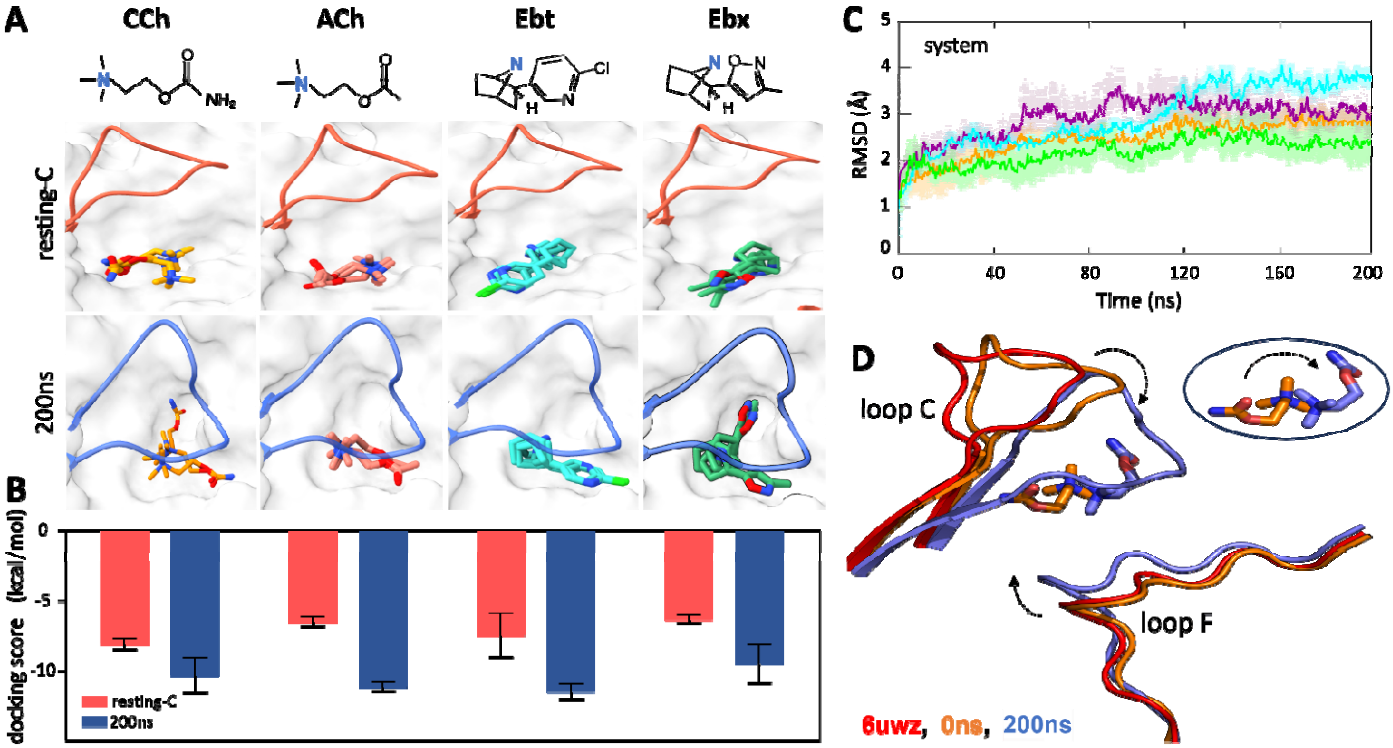

Figure 2. Agonist docking and loop dynamics. A. Top, agonists (blue, cationic center): carbamylcholine (CCh), acetylcholine (ACh), epibatidine (Ebt) and epiboxidine (Ebx). Bottom, $\alpha-\delta$ site with docked agonists (top 3 poses). Resting-C, 6UVW.pdb minus toxin (red): loop C is up and agonist is *cis;* 200 ns, after simulation and removal of CCh (blue): loop C is down and agonist is *trans*. B. Bottom, *for all 4 agonists the* docking scores (mean±SD, n=3) were more favorable after simulation. C. C_α RMSD (mean±SD, triplicates) are stable after ~120 ns (ACh, cyan; CCh, green; Ebt, orange; Ebx, purple). D. close-up of the CCh-occupied pocket. Red, resting-C; orange, equilibrated (0 ns MD); blue, after 200 ns MD. IN the simulations, loop C flops down (arrow), loop F moves in, the agonist flips *cis→trans* (circled inset).

182 *The L→H transition*. We performed 200 ns MD simulations for each of the resting-C docked complexes,
183 in triplicate (with different seed values). Videos 1 and 2 show simulations with CCh on 2 time scales,
184 expanded for the initial 200 ns and condensed for the full 1.0 μs. Video 3 shows a 200 ns simulation
185 with epiboxidine. The 200 ns simulations for all three replicates for all 4 agonists showed similar root-
186 mean-square-deviation (RMSD) patterns with differences consistently below 1Å (Figure 2C, Figure 2-
187 Source Data 1) suggesting that the trajectories were sufficiently robust and reproducible. Although
188 there were initial deviations, all systems became stable by ~120 ns. The root-mean-square-fluctuation
189 (RMSF) of the C_α atoms showed flexibility around the pocket mainly in loops C and F (but not E) (Figure
190 2-figure supplement 1). The fluctuations at the base of the ECD were anticipated because the TMD that
191 offers stability here was absent. However, there is no experimental evidence that the ECD-TMD
192 interfacial region influencing agonist binding energy, and (as described below) the match between
193 experimental binding energies (whole receptors) and those calculated in the simulations (ECD dimers)
194 further discounts this proposal. In addition, RMSD measurements show that, while agonists stabilize
195 binding pocket residues (compared to apo; Figure 2-figure supplement 2), interfacial residues continue
196 to fluctuate in the presence of agonists. The interfacial region plays an important role in setting the
197 unliganded gating equilibrium constant (L_0) but not agonist affinity (K_L or K_H).

198 In addition to the position changes of loops C and F during the simulations, in hold the ligand
199 orientation inverted, *cis→trans* (Figure 2D). For all ligands and in all trajectories, at the start of the
200 simulations the agonist's tail points towards the α subunit and at the end it points towards δ. This re-
201 orientation represents a nearly complete somersault (a 'flip') about the agonist's main cationic center
202 (N^+) that remains surrounded by the αW149-αY190-αY198 aromatic side chain cluster throughout (see
203 Figure 5; Figure 6-table supplement 1). The final MD configuration (with CCh) aligns well with the CCh-

204 bound cryo-EM desensitized structure (7QL6; RMSD <0.5 Å) (Figure 2-figure supplement 3). Video 2
205 shows that the final, *trans* orientation with CCh remains constant for at least 1 μs, indicating that
206 structure had settled by 200 ns with no further major rearrangements. This result is consistent with
207 functional measurements showing that D and O AChRs have indistinguishable affinities (citations in
208 (Auerbach, 2020)).

209 Additional results from MD simulations support the ECD dimer system as sufficient to model
210 the dynamics of the orthosteric site. First, the local rearrangements were similar in a ECD pentamer
211 docked with ACh to those in the dimer, including the *cis*→*trans* flip of agonist (Figure 2-figure
212 supplement 4). Second, 200 ns simulations of the apo ECD dimer show similar RMSF and RMSD
213 patterns to those with ligand present (CCh) (Figure 2-figure supplement 5A, 5B). Third, in these
214 simulations the downward displacement of loop C apparent with agonists (see below) was present, but
215 less pronounced (Figure 2-figure supplement 5C).

216 To test whether rearrangements in the simulations served to enforce the *trans* pose, we
217 removed the bound CCh from the final 200 ns MD structure and re-docked all 4 agonists. The preferred
218 poses for all were *trans* (Figure 2A, bottom). In the simulation, the preferred agonist orientation
219 switched from *cis* to *trans*. In addition, binding energies from docking scores were higher for the final
220 200 ns structures, consistent with an L-to-H transition (Figure 2B). Together, these results lead us to
221 propose that MD simulations may indeed reflect actual rearrangements of a neurotransmitter site in
222 the L-to-H, hold transition that turns on the AChR.

223

224 *Principal component analysis (PCA)*. To identify the most prominent conformational states of the
225 orthosteric site during the simulations, PCA was carried out based on the most significant fluctuations

226 (principal components). Considering the first two principal components (PC-1 and PC-2) that captured
227 the most pronounced C_α displacements (Figure 3-Source Data 1), backbone fluctuations revealed three
228 energy minima we call m1, m2, and m3 (Figure 3). The two most principal components accounted for
229 the majority of the variance, as indicated by the rapid decrease in the fraction of variance with
230 increasing eigenvalue rank (Figure 3-figure supplement 1). The consistency across different replicates
231 for all 4 agonists supports the convergence of the PCA analysis. To further assess this consistency, we
232 calculated the inner products of the top 10 principal components from each run. The resulting
233 heatmaps reveal the degree of similarity between runs, with the inner product values of PC-1 and PC-2
234 reflecting considerable overlap (50-90%) in the principal dynamic modes captured in each simulation
235 (Figure 3-figure supplement 2).

236 For all 4 agonists, all trajectories started in m1 and ended in m3, with m2 occurring as an
237 intermediate (Figure 3-figure supplement 3). The free energy landscapes as a function of PC1 and PC2
238 (Figure 3 and Figure 3-figure supplement 4) reveal variations in both the depths and variances of the
239 wells across different agonists. The well depths, derived from -kTlnρ values, reflect the frequency at
240 which each state is occupied during the simulation relative to other states. This, and the variance that
241 measures binding pose fluctuations around the mean positions for each minimum, provide insight into
242 structural stability. In general, pronounced wells were present for all three minima for all four agonists
243 (Figure 3-figure supplement 4). The only exception was m2 for ACh which was shallow, indicating a less
244 stable intermediate state between m1 and m3. For all agonists, the m3 pose was more localized and
245 stable compared to m1, with m2 being the least stable pose.

Pronounced fluctuations in loop C were evident in residue-wise RMSF plots and align well with the contributions of the first two principal components (PC-1 and PC-2) (Figure 2-figure

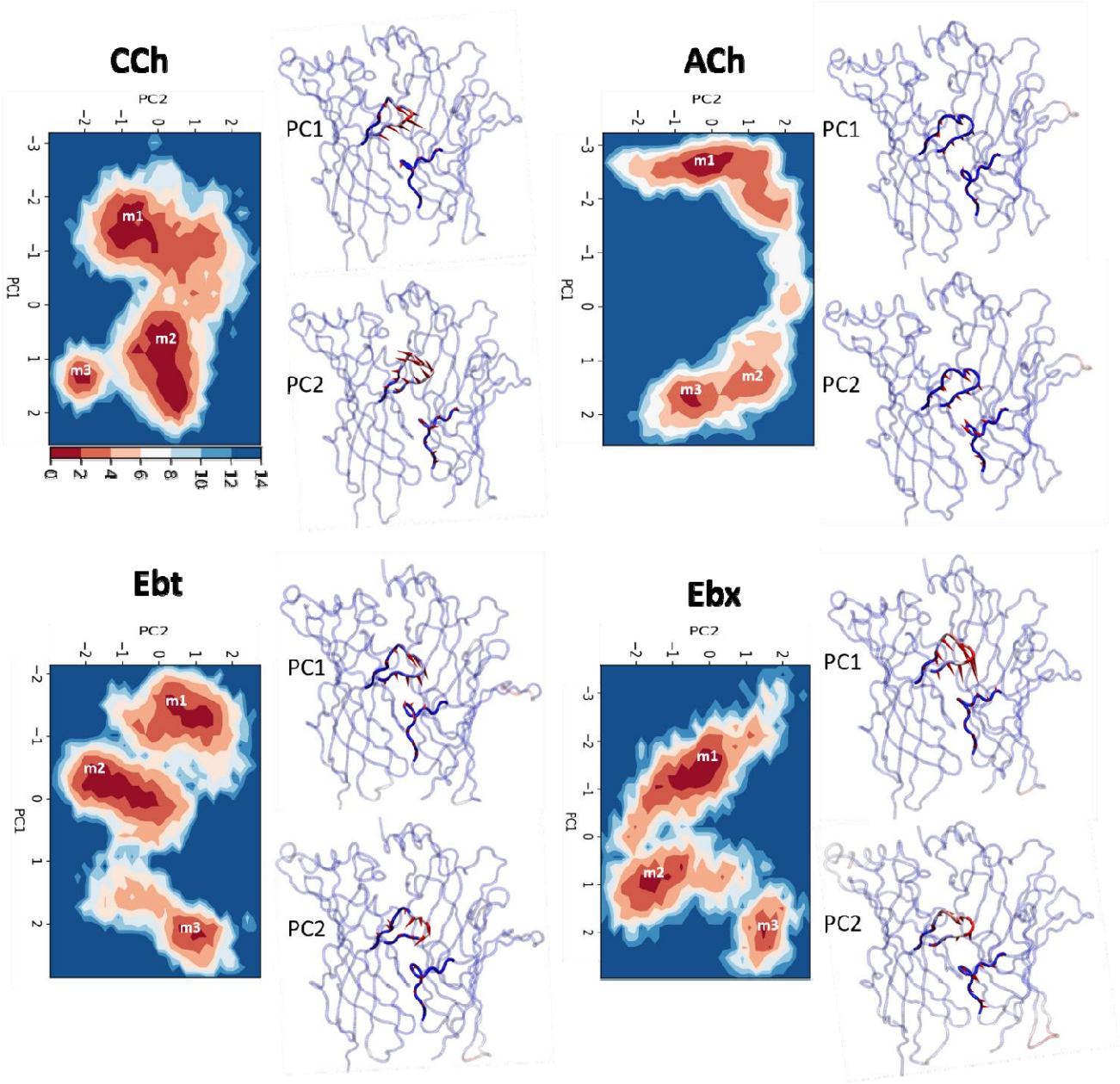

Figure 3. Principal Component Analysis (PCA). *Left,* for each agonist a plot of PC-1 versus PC-2, the first two principal components that capture the maximum variance in the trajectory (Figure 3-Source Data 1). Colors represent free energy value in kcal/mol (scale, upper left, bottom). For all agonists there are 3 energy minima (darkest red) - m1, m2, and m3 - that correspond to different conformations of the neurotransmitter site. *Right*, 'porcupine' plots indicating that the direction and magnitude of changes PC-1 versus PC-2 is in loops C and F. From energy comparisons (Figure 4, Figure 4-Source Data 1) and temporal sequences (Figure 3-figure supplement 2, Figure 4-Source Data 1) we hypothesize that m1 represent state AC_L, m3 represents state AC_H, and m2 is an intermediate state in the *L→H,* hold transition (Figure 1B).

256 supplement 5D). The apo and CCh occupied proteins adopt similar conformational spaces during the
257 200 ns simulation (Figure 2-figure supplement 5E). However, presence of the agonist appears to
258 increase conformational diversity, generating a broader distribution in the PCA plot. The bottom of the
259 m1, m2 and m3 energy wells in Figure 3 represent the most stable configurations of each population
260 and serve as reference points. In general (see next section), the ligand is *cis* m1 and *trans* in m3.

261 To further evaluate the stability of the binding poses in m1 and m3, we performed Binding Pose
262 Meta Dynamics (BPMD), an enhanced sampling method for assessing ligand stability in solution. The
263 BPMD calculations, which use CompositeScores derived from PoseScore (measuring ligand stability
264 based on RMSD) and PersScore (evaluating the persistence of key ligand-protein interactions). The
265 BPMD scores consistently showed lower scores for m3 compared to m1, indicating higher ligand
266 stability (Figure 3-figure supplement 5). Further, the *trans* orientation in m3 was more stable than *cis* in
267 m1, for all four ligands. Cross-docking of the *trans* orientation into the m1 conformation and the cis
268 orientation into the m3 conformation confirmed that these are the preferred orientations. BPMD
269 revealed that unstable ligand poses during the simulation are rarely occupied in the energy landscape
270 and therefore make minimal contributions to binding free energy.

271

272 *Computed versus experimental binding energies.* Although the well bottoms in Figure 3 represent the
273 most stable overall protein conformations, they do not directly convey information regarding agonist
274 stability or orientation. To incorporate this information, we performed a cluster analysis of the ligand
275 configuration using frames selected from the bottom of each PCA well as inputs. The top three
276 clusters, each having RMSD of ≤ 1.0 Å, shared a similar ligand orientation (Figure 3-figure supplement
277 3) and were selected to compute binding free energies (Figure 4, Figure 4-Source Data 1, Figure 4-

278 Source Data 2). The remaining frames were disregarded. The fraction of frames from each minimum
279 accepted for free energy calculations ranged from 20% (ACh, m1) to 71% (Ebt, m3). On average, the
280 fraction of frames selected was ~50%, showing the dynamic nature of the ligand in the pocket even in
281 the regions of overall stability (Videos 1 and 3).

282 The above procedure defined populations of structures that might represent the end states of
283 hold, AC_L (m1) and AC_H (m3), plus a previously unidentified intermediate state in the L→H transition
284 (m2). We used PBSA (Poisson-Boltzmann Surface Area) computations of the selected structures for
285 each agonist in each cluster population and compared the binding free energies calculated *in silico* with
286 real-world values measured previously *in vitro* by using electrophysiology (Indurthi & Auerbach, 2023).
287 PBSA is a computationally inexpensive method that provides a crude estimate of binding free energy
288 (Genheden & Ryde, 2015; Hou et al., 2011). Importantly, the PBSA method was used only as
289 fingerprint for identifying states rather than for free energy estimation. We already knew actual
290 binding free energies from the wet-bench experiments, so we used the PBSA values only to test the
291 hypothesis that m1 corresponds to L (ΔG_L) and m3 corresponds to H (ΔG_L).

292 The PBSA and experimental ΔG values are compared in Figure 4A left (Figure 4-Source Data 1).
293 For ACh and CCh, there was excellent agreement between ΔG_{m1} and ΔG_L and between ΔG_{m3} and ΔG_H.
294 The match was worse for the other 2 agonists, with the calculated values overestimating experimental
295 ones by ~45% (Ebt) and ~130% (Ebt). However, in all cases ΔG_{m3} was more favorable than ΔG_{m1}, and
296 the % overestimation compared to experimental values was approximately the same for m1 versus m3.
297 Overall, the PBSA-electrophysiology comparison supported the hypothesis that m1 represents AC_L and
298 m3 represents AC_H.

299 Further support for these assignments comes from comparing calculated vs experimental
300 efficiencies. Efficiency depends on the binding free energy *ratio*, $\Delta G_L/\Delta G_H$, rather than absolute ΔGs.
301 As described elsewhere, efficiency is the agonist's free energy change in hold relative to its total free
302 energy change in catch+hold (Nayak et al., 2019). It is the efficacy/high-affinity energy ratio, (ΔG_H-
303 ΔG_L)/ΔG_H or 1-($\Delta G_L/\Delta G_H$). Efficacy is the *amount*, and efficiency the *fraction*, of agonist binding energy
304 used to reduce the energy barrier separating L and H structures, to jumpstart gating.
305 Figure 4A right (Figure 4-Source Data 1) shows that efficiency values calculated *in silico* agreed
306 almost perfectly with those measured experimentally. This result is strong support for the hypothesis
307 that m1 represents AC_L and m3 represents AC_H. Further, it indicates that efficiency can be computed
308 accurately from structure alone. A possible reason for mismatches in ΔG but a match in efficiency is
309 given in the Discussion.
310 Together, the docking scores, matches in free energies and efficiencies, and alignment of
311 simulated m3 with cryo-EM desensitized structures support the hypothesis that MD simulations of a
312 single pdb file faithfully reproduce the end states of the hold rearrangement. Hence, the MD
313 trajectories likely reproduce the conformational dynamics of the orthosteric site in the initial stage of
314 gating, $AC_L \rightarrow AC_H$ (Figure 1B). This is the critical step that lowers the main barrier to activation of the
315 allosteric site, to promote the otherwise unfavorable gating isomerization.
316 Figure 4B shows some structural parameters of the orthosteric pocket, L (m1) versus H (m3). All
317 agonists showed an increase in Van der Waals (VdW) interaction energy in the hold rearrangement.
318 This confirms the previous suggestion that L→H restructuring generates a smaller, more-tightly packed
319 pocket (Tripathy et al., 2019). The calculated (PBSA) increase was most pronounced with Ebt and least

320 for Ebx, with CCh and ACh falling in between (Figure 4-Source Data 2). A compaction of the pocket is
321 also apparent in Figure 4C that shows a reduction in binding pocket volume, and in Figure 4D that
322 shows a decrease in the number of water molecules. As described below, the VdW contacts that form
323 concomitant to the agonist flip and loop C flop establish a more compact, hydrophobic and stable local
324 environment.
325
326

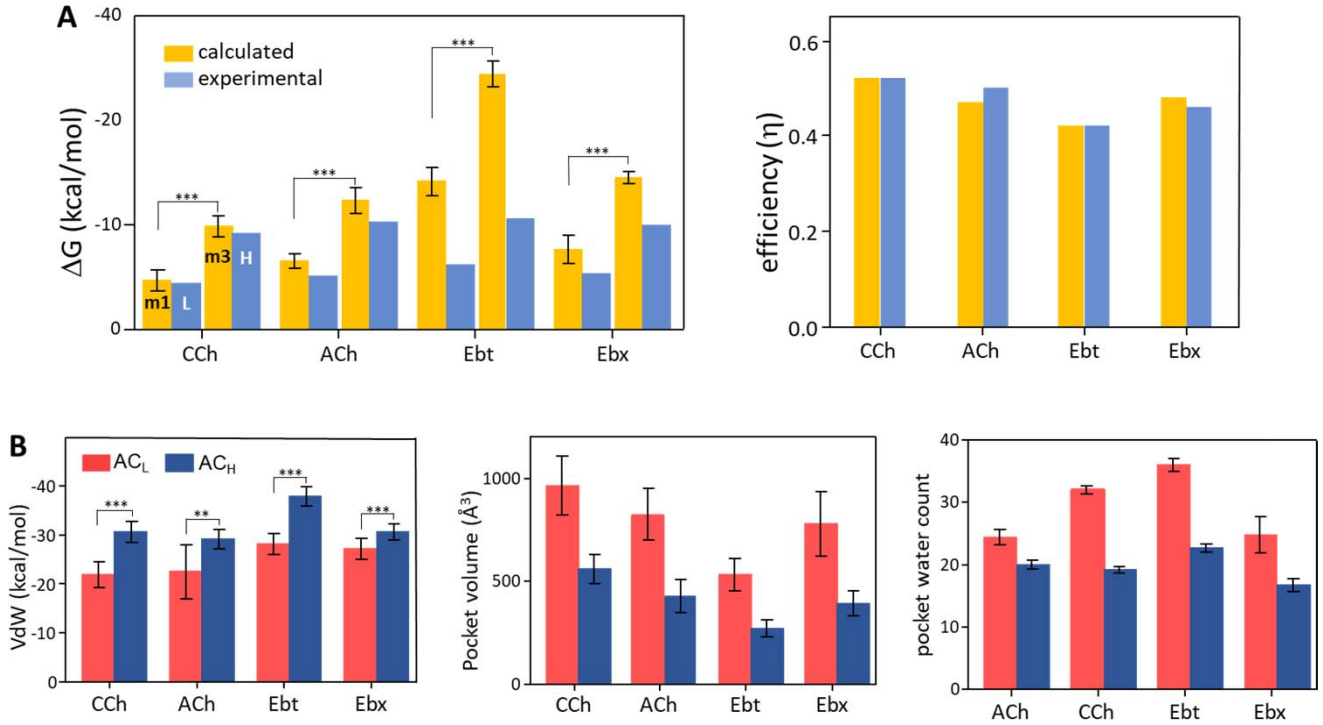

Figure 4. Binding free energies and pocket properties. A. Calculated (yellow) versus experimental (blue) binding free energies for 4 agonists (structures in Figure 2A, top) (Figure 4-Source Data 1). PBSA calculations were done on clusters selected from m1 and m3 minima of PCA plots (Figure 3; Figure 3-figure supplement 2). Left, absolute ΔG and right, efficiency (1- $\Delta G_L/\Delta G_H$). The agreement in efficiencies supports the hypothesis that m1 represents AC_L and m3 represents AC_H B. In L→H (red→blue), VdW interactions (left) increase, pocket volume (center) decreases, and the number of water molecules in the pocket (right) decreases. Overall, the pocket stabilizes, compacts and de-wets.

335 *Flip-Flop-Fix*. In L→H, the *cis→trans* rotation of the agonist was prominent in all simulations (Figure 5).
336 On average, the ligands underwent a >130° rotation about the N^+-αW149 fulcrum (Figure 1D). Also, in
337 all instances the flip began at the start of the simulation (m1).

338 A second consistent and prominent L→H restructuring event was the downward displacement
339 (flop) of loop C toward the pocket center, defined as the C_α of αW149. This well-known 'clamshell
340 closure' motion is conserved in related binding proteins (and in other receptors) and thought to play a
341 role in AChR activation by agonists (Basak et al., 2020; Hansen et al., 2005; Hibbs et al., 2009). In the
342 simulations, loop C flop was measured as the displacement of its tip (C_α of αC192) in m3 relative to its
343 apo position. The distance traveled varied with the agonist (Figure 6-table supplement 1) but we do
344 not discern a pattern in the extent of loop C flop with regard to agonist affinity, efficacy or efficiency.

345 In hold, residues that form the pocket cavity move, presumably to accommodate the reoriented
346 ligand. In L, αY190, αY93, and δW57 are spaced apart, providing an open slot that accommodates the
347 agonist's tail in the *cis* orientation (Figure 5- figure supplement 1). However, in H loop C flop
348 repositions αY190 closer to αY93, effectively filling the gap to create a unified surface.

349

350

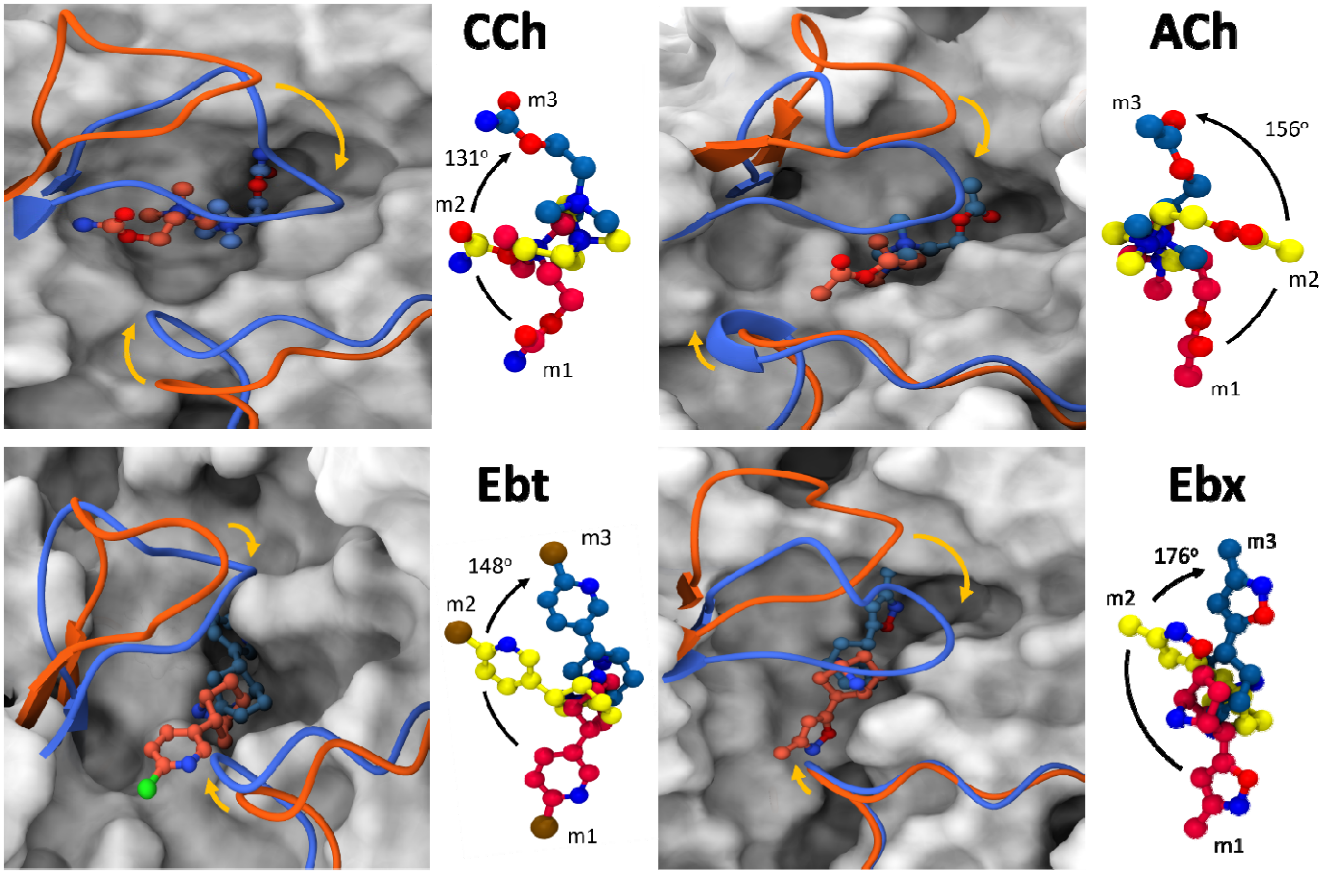

Figure 5. Agonist and loop movements in hold (flip and flop). A. *Left*, superimposed cartoons of AC_L (m1; orange) and AC_H (m3; blue). Loop C is upper left and loop F is lower right. In L→H (orange→blue) there is a *cis→trans* reorientation of the agonist (flip) and a downward movement of loop C (flop, arrow). R*ight*, agonist structure m1 (red) versus m2 (yellow) versus m3 (blue). Degree pertains to the m1→m3 rotation angle.

358 In the desensitized H structure, αW149, αY190, αY198 and (to a lesser extent) αY93 and δW57A
359 rings surround the agonist N^+ (Figure 1D). In adult-type mouse AChRs, substitutions of the 3 closest
360 aromatic residues have somewhat different consequences. With ACh, deleting the ring (A versus W at
361 149, A versus to F for 190 and 198) results in a loss (kcal/mol) of 3.0, 0.9, 2.1 for ΔG_L and 5.3, 2.8, 4.0
362 for ΔG_H, respectively (Purohit et al., 2014). αW149 (in loop B) is the main player in both L and H, but
363 the biggest binding energy increase in hold comes from αY190 (in loop C). αW149 makes a cation-π
364 bond with N^+ that is important for ligand stabilization (Xiu et al., 2009; Zhong et al., 1998). In the
365 simulations, the distance between these main aromatic groups and N^+ decreases only slightly, L→H
366 (Figure 6, Figure 6-table supplement 1). This aromatic cluster appears to act as a slippery anchor (a ball
367 joint) that maintains stability of the N^+ position even as the tail rotates within it, approximately
368 doubling agonist binding energy. The special role of αY190 is considered, below.
369 In AChBP (perhaps L), the hydroxyl group of αY93 forms a hydrogen bond with the ligand's head
370 group (Celie et al., 2004; Hansen et al., 2005). In the AChR L structure, the agonist's *cis* orientation
371 appears to be stabilized by this hydroxyl that is close to a functional group on the agonist's tail.
372 Likewise, the tail nitrogen in CCh, Ebt, and Ebx (amide or amine) forms a hydrogen bond with the
373 hydroxyl group of αY198, but only in the intermediate m2 state. This interaction may guide the
374 rotation and provide transient stability. The absence of a secondary nitrogen in ACh possibly explains
375 its alternate re-orientation route, as only this ligand was observed to flip counterclockwise (Figure 5). It
376 may also explain why the m2 basin in the PCA plots for ACh is especially broad and shallow (Figure 3).
377 The L→H transition compacts, de-wets and stabilizes the binding cavity (Figure 4; Videos 1-3). In
378 H, the tail functional moiety (carbonyl or secondary ring amine) in the *trans* orientation is sandwiched
379 between αC192, αC193 and αY198 (loop C), αT150 (loop B) and δC108, δN109, δL111 and δL121 (loop

380 E) (Figure 6- figure supplement 1). As reported elsewhere (Blum et al., 2010; Rahman et al., 2020;
381 Zarkadas et al., 2022), in our simulated H structure the functional group found in the tail of each
382 agonist -- the carbonyl group in CCh and ACh and the secondary ring amine in Ebt and Ebx - forms a
383 hydrogen bond with the carbonyl of δN109 and amine of δL121 in the complementary δ subunit
384 backbone *via* a structural water (Figure 6). The agonist's flip starts the m1→m2 transition, and the
385 establishment of this water-mediated H-bond completes in m2→m3 (Figure 6) (Video 2). This water-
386 mediated bonding and the increase in VdW interactions appear to both be crucial for stabilizing the
387 loops and agonist in the HA conformation of the neurotransmitter site.
388
389 *Salt-bridge*. Near the pocket, a αK145-αD200 salt bridge (Figure 1D) has been suggested to play an
390 important role in receptor activation (Beene et al., 2002; Gay & Yakel, 2007; Mukhtasimova et al.,
391 2005; Padgett et al., 2007; Pless et al., 2011). In the simulations, the rearrangement at αK145 are
392 complex and agonist dependent. In AC_H, this residue i) makes an apparent contact with αY93, ii) is
393 approached by the αY190 hydroxyl group (Figure 6-table supplement 1) and iii) loop F of the
394 complementary subunit.
395 Interestingly, the mutation αK145A lowers the efficiencies of ACh and CCh (from 0.51 to 0.41)
396 but has no effect on those of Ebt and Ebx (that remain at 0.41 and 0.46) (Indurthi & Auerbach, 2023).
397 This agonist dependence in function has a parallel in structure. In the hold simulations, the αK145-
398 αD200 distance (Å) increases from only 4.4 in apo to 6.1 or 5.1 in AC_L (CCh or ACh). This spreading may
399 relate to the agonist's tail being inserted into the αY93 slot in the *cis* orientation. In AC_L→AC_H, with ACh
400 and CCh the αK145-αD200 separation (Å) shortens substantially to 2.8 or 2.6, making it more rigid.
401 However, with Ebt and Ebx the αK145-αD200 distance remains unstable, fluctuating between 3-6 Å

throughout the course of the simulation. Likewise, αK145-αY190 distance stabilizes at 5.3 Å or 6.1 Å in AC_H with ACh and CCh but continues to fluctuate with Ebt and Ebx. In contrast, the αY190-αD200 distance remains stable in AC_H for all ligands. This suggests that the instability in the αK145-αD200 and αK145-αY190 distances can primarily be attributed to αK145 (Figure 6- figure supplement 2).

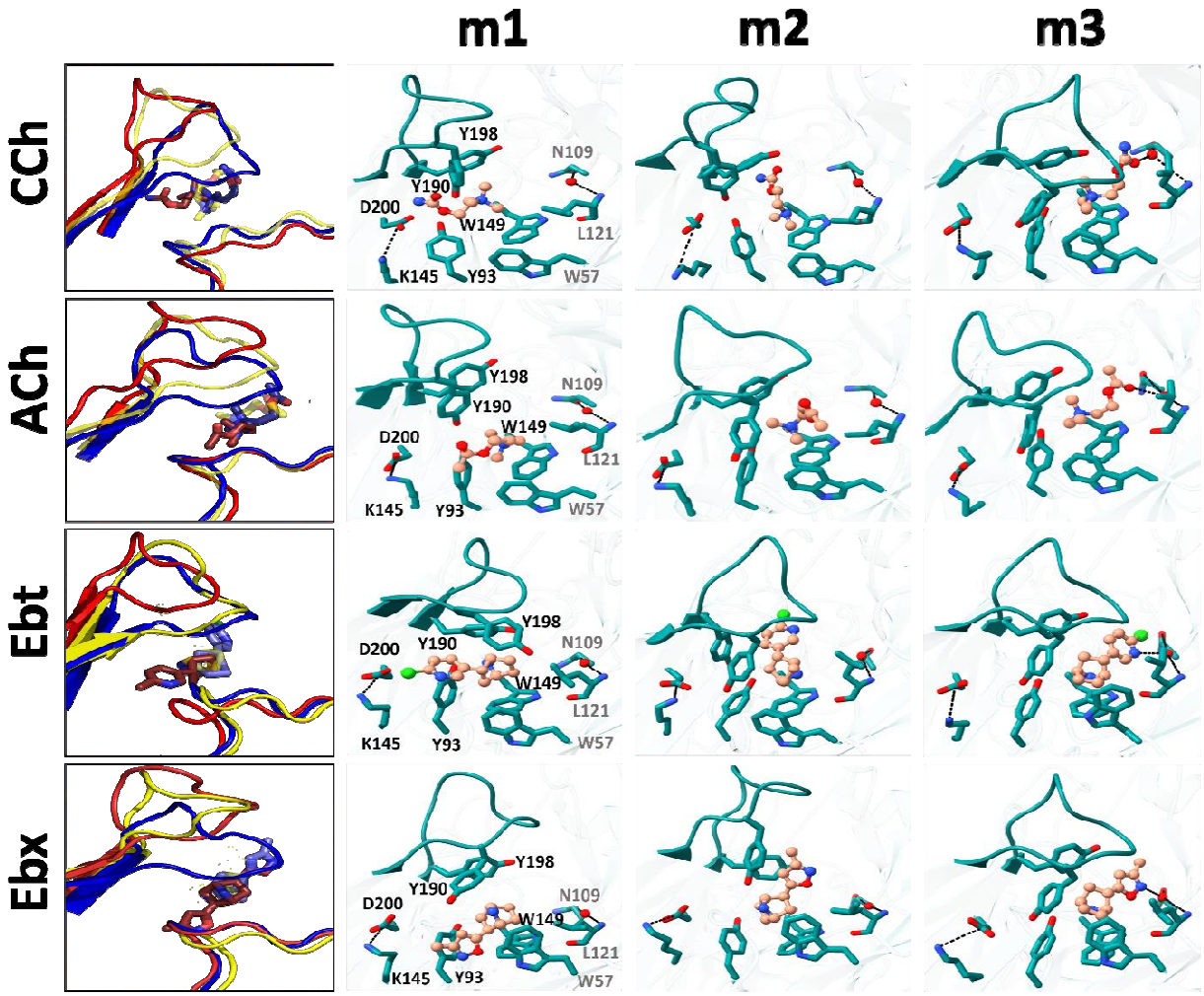

Figure 6: Representative snapshots in L→H (hold). *Left*, rearrangements of loop C, loop F and the ligand (red, m1; yellow, m2; blue, m3); *right*, residue and ligand orientations. m1 is AC_L, m2 is an intermediate state, m3 is AC_H. (Figure 1B). In m1, a functional group in the agonist tail interacts with αY93 (all agonists) and αD200 (only CCh and Ebt). The position and orientation of αW149 relative to N^+ of the agonist remains nearly unchanged m1→m2→m3 and serves as a fulcrum for the *cis*→*trans* flip (see Figure 5). In m2, the functional nitrogen at the agonist tail (CCh, Ebt and Ebx) interacts with the hydroxyl group of αY198. For all ligands, αY190 repositioning and loop C flop (m1→m3) are correlated. In m3, the agonist fully flips to *trans*, facilitating VdW interactions, de-wetting, and the formation of water-mediated hydrogen bonds with the reactive group at its tail with δN109/δL121 backbone (loop E) *via* a structural water.

416 **Discussion**

417 AChRs are typical allosteric proteins (Changeux, 2013). Electrophysiology experiments indicate
418 that agonists promote AChR activity by interacting with orthosteric sites in stages called touch-catch-
419 hold (Auerbach, 2024). We used MD simulations to probe structural changes in the hold
420 rearrangement that animates the protein. By comparing binding energies calculated *in silico* with those
421 measured *in vitro* we could identify provisionally in MD trajectories the end states AC_L and AC_H, plus an
422 intermediate configuration not detected in experiments. The conspicuous hold rearrangements
423 discussed below are a *cis*→*trans* rotation of the agonist (flip), an up→down displacement of loop C
424 (flop), and decreases in pocket volume, water content and loop fluctuations (fix).

425 Simulations require simplifications and are useful only insofar as they suggest experiments.
426 Hence, we emphasize the rearrangements discussed below are hypotheses that need to be tested.
427 Nonetheless, the agreements between cryo-EM (apo and desensitized) versus simulated (apo and C_H)
428 structures, and between ΔG_L and ΔG_H estimated from electrophysiology versus simulations, support
429 the hypothesis that the m1 and m3 conformations in the simulations reflect AC_L and AC_H structures. At
430 present there are no structures that correspond unambiguously to either of the hold end states, or to
431 the intermediate m2 state. Absent these, we can only offer flip, flop and fix as possibilities that can be
432 tested.

433 There was reasonably good agreement between calculated and experimental absolute binding
434 free energies for ACh and CCh (but not Ebt and Ebx), but the match was almost perfect for all ligands
435 when free energy ratios (efficiencies) were compared (Figure 4A). *In silico*, the absolute values
436 overestimated the experimental ones by approximately the same factor (different for each ligand) that,
437 however, cancelled in the ratio. We do not know the origin of this factor but speculate it could be

438 caused by errors in ligand parameterization. For example, using the same value for the Born radius of
439 nitrogen could overestimate ΔG more for ligands with azabicyclo versus quaternary ammonium
440 groups. Regardless, the results show that agonist efficiency can be estimated *in silico* and, therefore, in
441 the future could be a useful metric for analyzing dose-response curves and associating structure with
442 function. Further, excellent matches in energy measurements derived from pentamers
443 (electrophysiology) versus from ECD dimers (simulations) support the view that the ECD-TMD
444 interface, absent *in silico*, is not an important determinant of agonist affinity. Rather, these matches
445 are consistent with experiments that show that affinity is determined only by structural elements
446 within ~12 Å of the ligand (Gupta et al., 2017), and that the AChR orthosteric sites operate
447 independently (Nayak & Auerbach, 2017).
448
449 <u>*Summary*</u>. MD simulations of the α–δ AChR neurotransmitter site indicate the following back-and-
450 forth, generic sequence of rearrangements in $AC_L \rightarrow AC_H$ (Videos 1, 2 and 3).
451 **1. AC_L (m1)**: Agonist is *cis*, loop C is up, pocket is wide/wet/wobbly;
452 agonist exits *cis*, starting a rotation about the N^+-αW149 fulcrum (flip);
453 loop C starts to move down towards this fulcrum (flop).
454 **2. Intermediate (m2)**<u>:</u> Agonist is ~half-rotated with tail stabilized by αY198;
455 agonist completes rotation to *trans* but with the tail not secured in the pocket;
456 loop C moves down fully, to de-wet the pocket and deploy αY190 towards the salt bridge.
457 **3. AC_H (m3):** Agonist is *trans*, tail is secured by VdW contacts, an H-bond with structural water
458 (fix);. the pocket is narrow/dry/rigid.

459 Below, we consider the main structural elements associated with flip-flop-fix, namely the agonist, loop
460 C and the overall pocket, respectively.
461
462 *Agonist.* With all agonists and in all simulations, the rotation of N^+ in a slippery, aromatic ball joint
463 (αW149-αY190-αY198) starts the L→H transition. Similar movements of bound ligands have been
464 identified in other proteins. In AMPA-type glutamate receptors, the neurotransmitter glutamate binds
465 in either of 2 poses, crystallographic or inverted (Yu et al., 2018). In one MD simulation these
466 interconverted, suggesting the bound ligand is not rigidly fixed (that is, T480-E705 might act as a
467 slippery anchor). Although the alternative poses were not associated with experimental binding
468 energies, the binding cleft is more closed in the crystallographic (presumably H) versus inverted
469 (possibly L) orientation. Thus, it is possible that the inverse orientations of glutamate apparent in
470 AMPA receptors is related to the flip of the agonist apparent in the AChR simulations.
471 Multiple ligand positions in binding pockets have also been reported in glycine receptors (Yu et
472 al., 2014), 5-HT3 receptors (Basak et al., 2020), δ-opioid receptors (Shang et al., 2016), HIV-1 protease
473 (Klei et al., 2007) and transthyretin (Klabunde et al., 2000). In enzymes, small bound substrate
474 movements are apparent in hexokinase (Bennett & Steitz, 1978) and alcohol dehydrogenase (Plapp,
475 2010). Hence, it may not be unusual for movement of a bound ligand to trigger an otherwise
476 unfavorable local rearrangement to drive a change in protein function, either catalysis or an
477 isomerization (an 'induced fit'; (Richard, 2022)). Not only do untethered ligands have the ability to
478 come and go, they can also reorient to change binding energy and, hence, the local environment that
479 couples to protein function.

480 In AChRs, the flip cannot pertain to all agonists. Some with high potency are perfectly
481 symmetrical and completely lack a tail (tetramethylammonium). Although we have not yet identified
482 in detail the specific dynamics that underpin ΔG_H, factors other than flip must contribute.

483 The PCA plots (Figure 3) show 3 populations, one of which (m2) occurs in time between m1
484 (AC_L) and m3 (AC_H) (Figure 3-figure supplement 2). In m2, the agonist's tail (CCh, Ebt and Ebx) interacts
485 with αY198, possibly to guide the clockwise rotation of the ligand and reduce the probability of a
486 return to the *cis* orientation. The PBSA calculations indicate that ΔG_{m2} (that does not have an
487 experimental correlate) is intermediate between ΔG_L and ΔG_H for ACh and CCh, but least stable for Ebt
488 and Ebx (Figure 4-Source Data 1). We do not know the structural basis for this difference nor do we
489 understand its significance.

490

491 *Loop C.* A number of previous observations place focus on the role of the downward displacement of
492 loop C in receptor activation. In ACh binding proteins, the extent correlates with agonist potency
493 (Basak et al., 2020; Du et al., 2015; Polovinkin et al., 2018) even if voltage-clamp fluorometry of other
494 receptors shows it to be similar with agonists and antagonists (Chang & Weiss, 2002; Munro et al.,
495 2019; Pless & Lynch, 2009).

496 In our simulations of the apo AChR (without an agonist), loop C flops partially to narrow the
497 aqueous connection between the bath and the pocket (Figure 2-figure supplement 2C). It is therefore
498 interesting that electrophysiology measurements show the agonist association rate constant (k_{on}) is
499 substantially *faster* (approaching the diffusion limit) and less correlated with potency to H versus L
500 conformations (Grosman & Auerbach, 2001; Nayak & Auerbach, 2017). That is, it appears that loop C
501 flop generates a *higher* affinity, but not by restricting the rate of agonist entry. All 4 agonists dock in

502 the *cis* orientation to L (wide entrance) versus the *trans* orientation to H (narrow entrance) (Figure 2B).
503 Agonists indeed bind weakly to *cis* versus *trans*, so it appears that a structural element(s) disfavors
504 adopting the *trans* pose when loop C is up. We speculate that in addition to narrowing the entrance,
505 the loop C flop and accompanying rearrangements serve to reduce this inhibition and allow the *trans*
506 orientation. To test this hypothesis, both the encounter complex (the starting state of catch) and
507 possible inhibiting structural elements need to be identified.

508 The movement of loop C toward the pocket center resembles the 'clamshell closure' apparent
509 at other receptor binding sites (Chen et al., 2017; Hansen et al., 2005; Hibbs & Gouaux, 2011).
510 However, in light of the k_{on} experimental results mentioned above, using 'closure' and 'capping' to
511 describe this motion is misleading because these words imply placing a lid (a steric barrier) over the
512 pocket that would be expected to reduce, not increase, the agonist association rate constant. Despite
513 the facts that loop C flop narrows the entrance and is correlated with higher affinity, electrophysiology
514 experiments indicate clearly that it does not restrict agonist entry. For this reason, we prefer the
515 functionally neutral words 'flop' and 'up/down' to describe loop C displacement and position.

516 Truncation of loop C eliminates activation by ACh but has almost no effect on unliganded
517 activation (Purohit & Auerbach, 2013). Interestingly, leaving only loop C residues αY190 and αY198 in
518 place retains activation by ACh. Apparently, repositioning of one (or both) of these aromatic side
519 chains that anchor N+ in the up→down displacement of loop C is sufficient to maintain activation by
520 the neurotransmitter, but not necessary for constitutive activity. Loop C flop may be essential for
521 activation by agonists but not for constitutive activation.

522 An Ala substitution of αY190 results in a large loss of ACh binding energy with about half
523 coming from the removal of the hydroxyl group (Purohit et al., 2014). In contrast, the mutations

524 αY198F and αY93F have essentially no effect on ACh binding energy. These results suggest that
525 repositioning αY190 consequent to loop C flop is important for activation by ACh (Figure 6). The αY190
526 ring fills the slot that opens next to αY93 when the agonist exits *cis*, preventing a return (Figure 5-
527 figure supplement 1).

528 Loop C flop positions the αY190 hydroxyl close to the αD200-αK145 salt bridge. It has been
529 proposed that this rearrangement triggers the AChR allosteric transition (Beene et al., 2002; Gay &
530 Yakel, 2007; Mukhtasimova et al., 2005; Padgett et al., 2007; Pless et al., 2011). In support of this
531 interaction, the mutation αK145A reduces ACh (and choline) binding energy substantially but has no
532 effect when the αY190 hydroxyl is absent (Bruhova & Auerbach, 2017). Also, in the simulations with
533 ACh the downward displacement of loop C positions this hydroxyl far (~5.0 Å) from αD200 and αK145
534 (Figure 6-table supplement 1). Although with different agonists there was no correlation between
535 these separations and the degree of loop C displacement, the gap was smaller with high- (ACh and
536 CCh) versus low-efficiency agonists (Ebt and Ebx). We sought, but did not find, structural water in this
537 gap. The αY190 hydroxyl is an important determinant of L and particularly H binding energy, but the
538 simulations have not revealed the mechanism.

539 In summary, the simulations confirm a αY190 hydroxyl-bridge interaction but do not reveal its
540 nature or consequence. Rather than triggering the gating transition, the αY190-bridge interaction may
541 serve mainly to stabilize the down position of loop C and, hence, the H pocket. Substrate-induced loop
542 displacements are known to deploy residues to enhance catalysis, for example in chymotrypsin (Ma et
543 al., 2005) and triosephosphate isomerase (Brown & Kollman, 1987; Nickbarg et al., 1988).
544 Repositioning αY190 by loop C flop could be analogous.

545

546 Pocket. Distances of the aromatic-N^+ anchor remain relatively constant in the hold transition (Figure 6,
547 Figure 6-table supplement 1). We hypothesize that either very small distance changes associated with
548 cation-π bonds are important, or that some of the extra favorable agonist binding energy in H is
549 generated somewhere else. For the agonists we examined, the rotation places the tail into the main
550 binding cavity (Figure 6-figure supplement 1) (Video 1) with *trans* orientation secured by VdW
551 interactions (dehydration), a hydrogen bond with a structural water bonded to the loop E backbone of
552 the complementary subunit, and, possibly, the αY190-salt bridge interaction. The net result to the
553 overall pocket is a reduction in volume (Figure 4C) and increase in stability of loops C and F (Figure 3).
554 In the simulations, the first two structural changes, distributed over the large surface area of
555 the cavity, were robust and consistent for all 4 agonists. Compact, hydrophobic binding pockets are
556 associated with functional activation in other ion channels (Furukawa et al., 2005; Sigel & Steinmann,
557 2012) and observed in other proteins including β2-adrenergic receptors, opioid receptors, and HIV-1
558 protease (Huang et al., 2015; Rasmussen et al., 2011; Wlodawer & Erickson, 1993). A future objective
559 is to quantify each source of increased binding energy with regards to the aromatic cluster, αY190 salt-
560 bridge interaction, general pocket restructuring and H-bond with structural water.
561
562 After hold. The next step In AChR gating is a rearrangement in the extracellular domain. In related
563 receptors, upon activation this domain becomes more compact and stable, a rearrangement called
564 'unblooming' (Sauguet et al., 2014; Taly et al., 2009). This restructuring echoes that of hold at the AChR
565 neurotransmitter site. It is possible that the L→H rearrangement of the pocket nucleates subsequent
566 restructuring of the extracellular domain, by connections that are now unknown.

567 In the complementary δ subunit (Figure 1D), loop E (β5-β6 strands) has been implicated in
568 ligand discrimination (Basak et al., 2020; Muroi et al., 2009; Pless & Lynch, 2009). The double mutation
569 F106L+S108C in the β2 subunit of the α4β2 nicotinic AChR subtype significantly decreases the action of
570 Ebt without altering that of ACh (Tarvin et al., 2017). In addition, loop E residues are responsible for the
571 binding energy differences $\alpha-\gamma$ versus $\alpha-\delta$ (Nayak et al., 2016) and reduce site instability caused by
572 loop C mutations (Vij et al., 2015). Although our simulations do not shed light on these matters, the
573 temporal sequence flip-flop-fix suggests that perturbation of the loop E backbone could also play a role
574 in downstream activation of the receptor.

575 Agonists belong to efficiency classes in which $\Delta G_L/\Delta G_H$ is the same for all members. So far 5
576 such classes have been identified experimentally in adult-type AChRs, indicating that also are 5 pairs of
577 AC_L/AC_H structural classes (Indurthi & Auerbach, 2023). Although in the simulations loops C and F
578 movements and salt bridge distances were agonist dependent, with only 4 ligands we cannot associate
579 any these rearrangements with efficiency classes. Additional simulations using more agonists and with
580 binding site mutations may lead to better understanding of the dynamics that underpin molecular
581 recognition in catch and protein animation in hold, and perhaps reveal the structural basis of their
582 linkage (Auerbach, 2024).

583

584 Implications. Several aspects of this work may have general implications. The L and H end states of
585 hold emerged from simulations of a single protein structure and were identified by comparing
586 experimental with binding energies calculated using an inexpensive, approximate method. If general,
587 this approach could be useful because at present cryo-EM structures of the short-lived AC_L states are
588 difficult to obtain. Agonist efficiency was calculated accurately from structure alone. This, too, could

589 be useful because efficiency allows affinity and efficacy to be calculated from each other (Indurthi &
590 Auerbach, 2021). Using MD to estimate efficiency could facilitate dose-response analysis and speed
591 drug discovery. Finally, the simulations suggest that a rotation the agonist turns on the receptor. It
592 makes sense that the protein's global conformational change starts with the movement of a newly
593 added structural element. This possibility can be tested by experiments.

594 **Materials and Methods**

595 **Hardware and Software.** All computational studies were carried out on a Linux Ubuntu 20.04 based
596 workstation with 126 GB RAM, 64 CPU cores, and two RTX A5000 24 GB GPU cards, as well as an
597 Ubuntu 20.04 based server equipped with 132 GB RAM, 96 CPU cores, and two RTX A5000 24 GB GPU
598 cards. The software utilized includes the Maestro release 2022-2 graphical user interface (GUI) of the
599 Schrödinger software suite (BioLuminate, Schrödinger, LLC, NY, USA), Amber22 (Case et al., 2005),
600 VMD 1.9.3 (Humphrey et al., 1996), ChemDraw Professional 15.1 (Purushotham et al., 2022), ChimeraX
601 (Pettersen et al., 2021), and PyMOL (PyMOL Molecular Graphics System, Version 2.0, Schrödinger, LLC).

602 **Protein preparation.** Agonist energy changes are approximately independent of energy changes in the
603 protein beyond the orthosteric pocket. In the simulations, we removed the transmembrane domain
604 and simulated only $\alpha-\delta$ subunit extracellular domain dimers. The AC_L starting structure of the hold
605 transition was resting C (PDB: 6UWZ) after toxin removal that is essentially the same as the apo
606 structure (Zarkadas et al., 2022) (Figure 1C). The 4 agonists we examined were acetylcholine (ACh),
607 carbamylcholine (CCh), epibatidine (Ebt) and epiboxidine (Ebx) (Figure 2A). These are of similar size
608 (MW 187, 183, 209 and 178, respectively) but have different affinities, efficacies and efficiencies (0.50,
609 0.52, 0.42, and 0.46, respectively) (Indurthi & Auerbach, 2023).

610 Protein preparation was conducted using the Protein Preparation Wizard (PPW) (Purushotham
611 et al., 2022) and OPLS4 force field. Bond orders were assigned to atoms based on the CCD database,
612 with zero bond orders given to bonded metals. Missing hydrogen atoms were inserted, and disulfide
613 bonds were placed appropriately. During preprocessing, structural refinement was performed with
614 Maestro's Prime utility, optimizing and adding any missing side chains and residues. Missing residues
615 were formulated by combining SEQRS information from the PDB files and optimized using Prime's

616 ePLOP module. The ionization state of all heterogeneous groups, including ligands, bound metals, and
617 charged amino acids, were determined using the EpiK tool at a pH range of 7.0 ± 2.0. Subsequent force
618 field minimization allowed for water sampling and basic restraint minimization, during which only
619 hydrogen atoms could be freely reduced.

620 The hydrogen bonding (H-bond) network underwent significant modification. The terminal chi
621 angle for residues Asn, Gln, and His was sampled through 180-degree flips, altering their spatial H-
622 bonding capabilities without affecting the fit to electron density. The neutral and protonated states of
623 His, Asp, and Glu, as well as two His tautomers, were sampled. Hydrogens on hydroxyls and thiols were
624 also analyzed to enhance the H-bond network. Finally, the ProtAssign method was employed in two
625 modes: a "regular" mode, which completed in seconds, and an "exhaustive" mode that considered
626 many more states and could take minutes or hours, depending on the H-bond network complexity.

627 **Ligand Preparation.** The two-dimensional SDF structures of CCh, ACh, Ebt and Ebx were retrieved from
628 the PUBCHEM database. These agonists were chosen because they have a similar size and represent
629 different efficiency classes (Indurthi & Auerbach, 2023). LigPrep (LigPrep, Maestro 11.2.014,
630 Schrödinger LLC) was utilized to construct ligands, produce stereoisomers, and generate tautomers
631 using the OPLS46 force field. Additionally, the Epik module was employed to desalt and protonate the
632 ligands at pH 7.0. Default values were applied to the remaining parameters, and LigPrep was also used
633 to prepare the ligands with the option "retain specified chiralities" engaged.

634 In terms of ligand state assessment, Epik can calculate a penalty to quantify the energy cost of
635 forming each state in solution based on the Hammett and Taft methods. This EpiK state penalty is
636 entirely compatible with the GlideScore used for docking, as it is computed in kcal/mol units. This
637 compatibility facilitates the examination of how the EpiK state penalty affects the GlideScore. The

638 DockingScore in Glide represents the total of the GlideScore and the Epik state penalty and served as
639 the basis for final ranking and enrichment evaluation. Furthermore, Epik offers a technique for
640 handling metal binding states, involving a change in the pH range within which the state is generated.
641 This approach underscores the comprehensive considerations made in preparing the ligands for
642 docking and subsequent analyses.

643 **Grid Generation and Molecular Docking.** The receptor grid complex of 6UWZ.pdb was generated after
644 removing alpha-bungarotoxin from the binding pocket using Glide (Glide, Maestro 11.2.014,
645 Schrödinger LLC). A virtual grid box with dimensions 20Å × 20Å × 20 Å was formed, centered within the
646 C and F loops in the α–δ binding site of the energy-minimized resting state. This grid box was used to
647 generate a receptor grid, and the default values were assigned for other parameters. Docking was
648 performed using the ligand docking wizard built into the Glide module of Schrödinger, with the default
649 scaling factor and partial charge cutoff set to 0.80 and 0.15, respectively. The docking procedure
650 consisted of two stages, extra precision (XP) followed by post-processing with prime MM-GBSA. The
651 best dock poses were selected based on dock score and MM-GBSA energy for further investigation.

652 **Molecular Dynamics Simulations.** MD simulations were conducted using the Amber22 software suite
653 within the Amber module as detailed elsewhere (Singh et al., 2021; Srivastava et al., 2022). Ligand
654 topology was prepared via the Leap module in AmberTools22, employing force field ff19SB (Tian et al.,
655 2020) and the Generalized Amber Force Field (GAFF) (Vassetti et al., 2019). The AM1BCC strategy and
656 GAFF2 were used to assign atomic charges and additional parameters. Before simulation, the systems
657 were minimized and equilibrated following a five-step minimization process, with each step involving
658 10,000 energy minimization steps. Systems were heated under NVT ensembles in two consecutive runs
659 from 0–300 K for 1 ns each, followed by a 1 ns simulation at 300 K and 1 bar pressure under the NPT

660 ensemble for equilibration. An additional 5 ns equilibration was performed before the 200 ns
661 production MD for each system, conducted under periodic boundary conditions (PBCs) and utilizing an
662 NPT ensemble with 300 K and 1 bar pressure. Long-range electrostatic interactions were treated using
663 the particle mesh Ewald method (PME), including a direct space cutoff of 12.0 Å and van der Waals
664 interactions. In production MD, a time step of 2.0 fs was employed, and the SHAKE algorithm was used
665 to keep bond lengths at equilibrium. Isobaric (NPT) conditions were maintained using the Berendsen
666 barostat, with temperature monitored by a Langevin thermostat. Coordinates from the production MD
667 were recorded in the trajectory file every 20 ps, resulting in a minimum of 10,000 frames. Trajectories
668 were analyzed using amber-tools CPPTRAJ (Roe & Cheatham, 2013), and further analysis and figure
669 generation were completed with VMD, Pymol, Xmgrace and ChimeraX. To ensure reproducibility, MD
670 trajectories were generated in triplicate.

671 **Cluster Analysis.** Cluster analysis of the ligand was performed using TCL scripts within the Visual
672 Molecular Dynamics (VMD) software, as described elsewhere (Mittal, Tonk, et al., 2021). In brief, this
673 script automates the identification of frames from the most stable conformations based on PCA
674 minima. Using these frames as input, the algorithm employed RMSD values of ligand positions to
675 cluster similar orientations. Specifically, clusters with an RMSD of ≤ 1Å were considered to share a
676 similar ligand orientation. Frames that did not fit into these top clusters were automatically excluded
677 by the script.

678 **Principal Component Analysis (PCA) and Free Energy Landscape (FEL).** PCA identifies collective
679 motions in atomic-level simulations of macromolecules (Mittal, Srivastava, et al., 2021; Srivastava et
680 al., 2022). It emphasizes significant patterns by reducing noise in MD simulations, revealing essential
681 dynamics underlying conformational changes. All equilibrated MD simulation trajectories were

682 analyzed by PCA computations using the CPPTRAJ algorithm using Amber tools. Prior to PCA, least-
683 square fitting of the protein's Cα atoms was carried out with respect to a reference structure (average
684 protein coordinates) to eliminate rotational and translational degrees of freedom in the simulation
685 box. A positional covariance matrix C (of dimensions $3N \times 3N$) was constructed using the Cα atom
686 coordinates, and this matrix was diagonalized to produce eigenvectors (directions of motion) and
687 eigenvalues (magnitudes). The elements of the covariance matrix C were obtained using:

688 $$C_i = \langle (X_i - \langle X_i \rangle)(X_j - \langle X_j \rangle) \rangle \quad (i, j=1,2,3.....,3N)$$

689 where X_i and X_j are the Cartesian coordinates of the Cα atoms, and N is the number of Cα atoms. The ⟨⟩
690 notation represents the ensemble average of atomic positions in Cartesian space. The resulting
691 principal components (eigenvectors) were sorted by the total motion they captured, generating 3N
692 eigenvectors. The free energy landscapes (FELs; Figure3) were created using the "g_sham" module in
693 GROMACS, based on the probability distribution of the top two principal components (PCs). The FEL
694 plot aids in visualizing possible conformations and corresponding energy levels. The free energy values
695 (G) were calculated as

696 $$G_i = -kT \ln(N_i/N_{max})$$

697 where k is the Boltzmann constant, T is the absolute temperature of the simulated system (300 K), N_i is
698 the population of bin i, and N_{max} is the population of the most-populated bin.

699 **Binding Pose Meta Dynamics (BPMD):** BPMD was performed using the Desmond module in
700 Schrodinger, involving 10 independent meta dynamics simulations of 10 ns each to improve statistical
701 reliability, with results averaged over the simulations. The collective variable (CV) was the RMSD of the
702 ligand heavy atoms relative to their starting positions, evaluated after superimposing the binding sites
703 to account for drift. The hill height and width were set at 0.05 kcal/mol and 0.02 Å, respectively. The

704 system was solvated in a 12.0 Å box and underwent several minimizations to slowly reach a
705 temperature of 300K, releasing any bad contacts or strain in the initial structure. Stability was assessed
706 in terms of ligand RMSD fluctuations (PoseScore) and the average persistence of important contacts,
707 such as hydrogen bonds and pi-pi interactions, between the ligand and protein residues (PersScore).
708 Higher PersScore values indicate more stable complexes, while lower PoseScore values indicate more
709 stable ligand positions. The CompositeScore (CompScore) combines these metrics, accounting for both
710 ligand drift and the persistence of protein/ligand hydrogen bonds. Lower CompScore values
711 correspond to more stable protein/ligand complexes.

712 **Binding Free Energy Calculation.** Experimental binding free energies were estimated by using
713 electrophysiology, as described elsewhere (Indurthi & Auerbach, 2023). Briefly, the constants K_L and L_2
714 (Figure 1B) were estimated from single-channels kinetics or dose-response curves, and K_H was
715 calculated using the thermodynamic cycle with L_0 known *a priori*. The logs of K_L and K_H are
716 proportional to ΔG_L and ΔG_H. The binding free energy of the protein-ligand docked complex (ΔG_{bind})
717 was calculated in two stages, after docking (using MM-GBSA in the Prime module of Schrödinger)
718 (Mittal, Tonk, et al., 2021; Purushotham et al., 2022) and after MD simulation on equilibrated MD
719 trajectories (using MM-PBSA/-GBSA in AMBER22). MM-PBSA is an approximation that can be useful to
720 compare binding affinities between different states and among agonists (Kollman et al., 2000; Rastelli
721 et al., 2010; Sun et al., 2014). In our use, MM-PBSA computations included both enthalpic (ΔH)
722 contributions from molecular interactions (van der Waals, electrostatics, solvation) and entropic ($T\Delta S$)
723 contributions calculated using normal mode analysis. By capturing the dynamic interplay between the

724 ligand and receptor as well as the influence of the surrounding solvent environment this approach
725 enables computation of a Gibbs free energy (ΔG).

726 After docking, for the static docked pose of the protein-ligand complex the MM-GBSA binding
727 energy calculation was performed using the OPLS4 force field and the variable-dielectric generalized
728 Born (VSGB) model in the Prime MM-GBSA module in Schrödinger 2022. We used ΔG_{bind_dock} to rank
729 protein-ligand docked complexes, selecting those with the highest negative values and dock scores as
730 the best ligands for further studies. After MD Simulation, in the MD equilibrated system binding
731 energies were calculated through the MM-PBSA/-GBSA protocol, implemented in AMBER22. This was
732 performed over the most stable clustered poses extracted from the equilibrated trajectory at minima
733 m1, m2, and m3 on the free energy landscape (FEL) over a 200 ns time frame. AMBER utilizes the
734 conventional g_mmpbsa module for MM-PBSA calculations using MM-PBSA.py script. These methods
735 calculate the energies of electrostatic interactions, van der Waals interactions, polar solvation, and
736 non-polar solvation in the equilibrated trajectory using a single trajectory protocol (STP). The binding
737 energy of each protein-ligand complex was calculated as $\Delta G_{bind}=\Delta G_{complex}-\Delta G_{protein}-\Delta G_{ligand}$,
738 where $\Delta G_{complex}$, $\Delta G_{protein}$, and ΔG_{ligand} represent the absolute free energies of the complex, protein, and
739 ligand systems, respectively. Additional terms, such as ΔH (enthalpy), T and ΔS (temperature and total
740 solute entropy), ΔG_{gas} (total gas phase energy), and ΔG_{solv} (solvation energy), contribute to the
741 calculation.

742 The Poisson-Boltzmann calculations were performed using an internal PBSA solver in Sander,
743 while Generalized Born ESURF was calculated using 'LCPO' surface areas. The vibrational mode entropy
744 contributions (TΔS) for protein-ligand interactions were calculated and averaged using normal-mode
745 analysis in Amber. The entropy term provides insights into the disorder within the system, as well as

746 how this disorder changes during the binding process. This value was added to the enthalpy term
747 computed by the MM-PBSA method to determine the absolute binding free energy (ΔG_{bind}). These
748 comprehensive calculations were used only as fingerprints for associating structures in simulations
749 with states defined by experimental (electrophysiology) free energy measurement (Figure 4A).
750 **Pocket Volume Calculation.** To investigate the variations in binding site volume across all four agonist-
751 bound cases, pocket volume analysis was carried out using POVME3.0 (Wagner et al., 2017). From each
752 of the four systems, frames were extracted at consistent intervals with a stride of 2.0, culminating in
753 representative sets of 5000 protein structures for every system. Before commencing the volume
754 calculation, the trajectory was aligned, and frames were selected from VMD, serving as the initial input
755 for this method. Subsequently, an inclusion region was defined, encapsulating all binding pocket
756 conformations within the trajectory. This region's definition involved building a sphere upon which the
757 inclusion grid-points were computed, using different atoms of the ligand for this calculation.
758

759 **References:**

760 Auerbach, A. (2020). Pathways for nicotinic receptor desensitization. *J Gen Physiol*, *152*(10).
761 https://doi.org/10.1085/jgp.202012639
762 Auerbach, A. (2024). Dynamics of receptor activation by agonists [Perspective]. *Biophysical Journal*,
763 *123* (15). https://doi.org/https://doi.org/10.1016/j.bpj.2024.01.003
764 Basak, S., Kumar, A., Ramsey, S., Gibbs, E., Kapoor, A., Filizola, M., & Chakrapani, S. (2020). High-
765 resolution structures of multiple 5-HT(3A)R-setron complexes reveal a novel mechanism of
766 competitive inhibition. *Elife*, *9*. https://doi.org/10.7554/eLife.57870
767 Beene, D. L., Brandt, G. S., Zhong, W., Zacharias, N. M., Lester, H. A., & Dougherty, D. A. (2002). Cation-
768 pi interactions in ligand recognition by serotonergic (5-HT3A) and nicotinic acetylcholine
769 receptors: the anomalous binding properties of nicotine. *Biochemistry*, *41*(32), 10262-10269.
770 https://doi.org/10.1021/bi020266d
771 Bennett, W. S., Jr., & Steitz, T. A. (1978). Glucose-induced conformational change in yeast hexokinase.
772 *Proc Natl Acad Sci U S A*, *75*(10), 4848-4852. https://doi.org/10.1073/pnas.75.10.4848
773 Blum, A. P., Lester, H. A., & Dougherty, D. A. (2010). Nicotinic pharmacophore: the pyridine N of
774 nicotine and carbonyl of acetylcholine hydrogen bond across a subunit interface to a backbone
775 NH. *Proc Natl Acad Sci U S A*, *107*(30), 13206-13211. https://doi.org/10.1073/pnas.1007140107
776 Brown, F. K., & Kollman, P. A. (1987). Molecular dynamics simulations of "loop closing" in the enzyme
777 triose phosphate isomerase. *J Mol Biol*, *198*(3), 533-546. https://doi.org/10.1016/0022-
778 2836(87)90298-1
779 Bruhova, I., & Auerbach, A. (2017). Molecular recognition at cholinergic synapses: acetylcholine versus
780 choline. *J Physiol*, *595*(4), 1253-1261. https://doi.org/10.1113/JP273291
781 Case, D. A., Cheatham, T. E., 3rd, Darden, T., Gohlke, H., Luo, R., Merz, K. M., Jr., Onufriev, A.,
782 Simmerling, C., Wang, B., & Woods, R. J. (2005). The Amber biomolecular simulation programs.
783 *J Comput Chem*, *26*(16), 1668-1688. https://doi.org/10.1002/jcc.20290
784 Celie, P. H., van Rossum-Fikkert, S. E., van Dijk, W. J., Brejc, K., Smit, A. B., & Sixma, T. K. (2004).
785 Nicotine and carbamylcholine binding to nicotinic acetylcholine receptors as studied in AChBP
786 crystal structures. *Neuron*, *41*(6), 907-914. https://doi.org/10.1016/s0896-6273(04)00115-1
787 Chang, Y., & Weiss, D. S. (2002). Site-specific fluorescence reveals distinct structural changes with
788 GABA receptor activation and antagonism. *Nat Neurosci*, *5*(11), 1163-1168.
789 https://doi.org/10.1038/nn926
790 Changeux, J. P. (2013). The concept of allosteric modulation: an overview. *Drug Discov Today Technol*,
791 *10*(2), e223-228. https://doi.org/10.1016/j.ddtec.2012.07.007
792 Chen, S., Zhao, Y., Wang, Y., Shekhar, M., Tajkhorshid, E., & Gouaux, E. (2017). Activation and
793 Desensitization Mechanism of AMPA Receptor-TARP Complex by Cryo-EM. *Cell*, *170*(6), 1234-
794 1246 e1214. https://doi.org/10.1016/j.cell.2017.07.045
795 Cymes, G. D., & Grosman, C. (2021). Signal transduction through Cys-loop receptors is mediated by the
796 nonspecific bumping of closely apposed domains. *Proc Natl Acad Sci U S A*, *118*(14).
797 https://doi.org/10.1073/pnas.2021016118
798 Du, J., Lu, W., Wu, S., Cheng, Y., & Gouaux, E. (2015). Glycine receptor mechanism elucidated by
799 electron cryo-microscopy. *Nature*, *526*(7572), 224-229. https://doi.org/10.1038/nature14853
800 Furukawa, H., Singh, S. K., Mancusso, R., & Gouaux, E. (2005). Subunit arrangement and function in
801 NMDA receptors. *Nature*, *438*(7065), 185-192. https://doi.org/10.1038/nature04089

802 Gay, E. A., & Yakel, J. L. (2007). Gating of nicotinic ACh receptors; new insights into structural
803 transitions triggered by agonist binding that induce channel opening. *J Physiol*, *584*(Pt 3), 727-
804 733. https://doi.org/10.1113/jphysiol.2007.142554
805 Genheden, S., & Ryde, U. (2015). The MM/PBSA and MM/GBSA methods to estimate ligand-binding
806 affinities. *Expert Opin Drug Discov*, *10*(5), 449-461.
807 https://doi.org/10.1517/17460441.2015.1032936
808 Grosman, C., & Auerbach, A. (2001). The dissociation of acetylcholine from open nicotinic receptor
809 channels. *Proc Natl Acad Sci U S A*, *98*(24), 14102-14107.
810 https://doi.org/10.1073/pnas.251402498
811 Grosman, C., Zhou, M., & Auerbach, A. (2000). Mapping the conformational wave of acetylcholine
812 receptor channel gating. *Nature*, *403*(6771), 773-776. https://doi.org/10.1038/35001586
813 Gupta, S., Chakraborty, S., Vij, R., & Auerbach, A. (2017). A mechanism for acetylcholine receptor
814 gating based on structure, coupling, phi, and flip. *J Gen Physiol*, *149*(1), 85-103.
815 https://doi.org/10.1085/jgp.201611673
816 Hansen, S. B., Sulzenbacher, G., Huxford, T., Marchot, P., Taylor, P., & Bourne, Y. (2005). Structures of
817 Aplysia AChBP complexes with nicotinic agonists and antagonists reveal distinctive binding
818 interfaces and conformations. *Embo Journal*, *24*(20), 3635-3646.
819 https://doi.org/10.1038/sj.emboj.7600828
820 Hibbs, R. E., & Gouaux, E. (2011). Principles of activation and permeation in an anion-selective Cys-loop
821 receptor. *Nature*, *474*(7349), 54-60. https://doi.org/10.1038/nature10139
822 Hibbs, R. E., Sulzenbacher, G., Shi, J., Talley, T. T., Conrod, S., Kem, W. R., Taylor, P., Marchot, P., &
823 Bourne, Y. (2009). Structural determinants for interaction of partial agonists with acetylcholine
824 binding protein and neuronal alpha7 nicotinic acetylcholine receptor. *Embo Journal*, *28*(19),
825 3040-3051. https://doi.org/10.1038/emboj.2009.227
826 Hou, T., Wang, J., Li, Y., & Wang, W. (2011). Assessing the performance of the MM/PBSA and
827 MM/GBSA methods. 1. The accuracy of binding free energy calculations based on molecular
828 dynamics simulations. *Journal of Chemical Information and Modeling*, *51*(1), 69-82.
829 https://doi.org/10.1021/ci100275a
830 Huang, W., Manglik, A., Venkatakrishnan, A. J., Laeremans, T., Feinberg, E. N., Sanborn, A. L., Kato, H.
831 E., Livingston, K. E., Thorsen, T. S., Kling, R. C., Granier, S., Gmeiner, P., Husbands, S. M.,
832 Traynor, J. R., Weis, W. I., Steyaert, J., Dror, R. O., & Kobilka, B. K. (2015). Structural insights into
833 micro-opioid receptor activation. *Nature*, *524*(7565), 315-321.
834 https://doi.org/10.1038/nature14886
835 Humphrey, W., Dalke, A., & Schulten, K. (1996). VMD: visual molecular dynamics. *J Mol Graph*, *14*(1),
836 33-38, 27-38. https://doi.org/10.1016/0263-7855(96)00018-5
837 Indurthi, D., & Auerbach, A. (2021). Agonist Efficiency Estimated from Concentration Response Curve.
838 *Biophysical Journal*, *120*(3), 57a-57a. <Go to ISI>://WOS:000629601400276
839 Indurthi, D. C., & Auerbach, A. (2023). Agonist efficiency links binding and gating in a nicotinic receptor.
840 *Elife*, *12*. https://doi.org/10.7554/eLife.86496
841 Jackson, M. B. (1986). Kinetics of unliganded acetylcholine receptor channel gating. *Biophys J*, *49*(3),
842 663-672. https://doi.org/10.1016/S0006-3495(86)83693-1
843 Jackson, M. B. (1989). Perfection of a synaptic receptor: kinetics and energetics of the acetylcholine
844 receptor. *Proc Natl Acad Sci U S A*, *86*(7), 2199-2203. https://doi.org/10.1073/pnas.86.7.2199

845 Jadey, S., & Auerbach, A. (2012). An integrated catch-and-hold mechanism activates nicotinic
846 acetylcholine receptors. *J Gen Physiol*, *140*(1), 17-28. https://doi.org/10.1085/jgp.201210801
847 Klabunde, T., Petrassi, H. M., Oza, V. B., Raman, P., Kelly, J. W., & Sacchettini, J. C. (2000). Rational
848 design of potent human transthyretin amyloid disease inhibitors. *Nat Struct Biol*, *7*(4), 312-321.
849 https://doi.org/10.1038/74082
850 Klei, H. E., Kish, K., Lin, P. F., Guo, Q., Friborg, J., Rose, R. E., Zhang, Y., Goldfarb, V., Langley, D. R.,
851 Wittekind, M., & Sheriff, S. (2007). X-ray crystal structures of human immunodeficiency virus
852 type 1 protease mutants complexed with atazanavir. *J Virol*, *81*(17), 9525-9535.
853 https://doi.org/10.1128/JVI.02503-05
854 Kollman, P. A., Massova, I., Reyes, C., Kuhn, B., Huo, S., Chong, L., Lee, M., Lee, T., Duan, Y., Wang, W.,
855 Donini, O., Cieplak, P., Srinivasan, J., Case, D. A., & Cheatham, T. E., 3rd. (2000). Calculating
856 structures and free energies of complex molecules: combining molecular mechanics and
857 continuum models. *Acc Chem Res*, *33*(12), 889-897. https://doi.org/10.1021/ar000033j
858 Ma, W., Tang, C., & Lai, L. (2005). Specificity of trypsin and chymotrypsin: loop-motion-controlled
859 dynamic correlation as a determinant. *Biophys J*, *89*(2), 1183-1193.
860 https://doi.org/10.1529/biophysj.104.057158
861 Mittal, L., Srivastava, M., Kumari, A., Tonk, R. K., Awasthi, A., & Asthana, S. (2021). Interplay among
862 Structural Stability, Plasticity, and Energetics Determined by Conformational Attuning of
863 Flexible Loops in PD-1. *Journal of Chemical Information and Modeling*, *61*(1), 358-384.
864 https://doi.org/10.1021/acs.jcim.0c01080
865 Mittal, L., Tonk, R. K., Awasthi, A., & Asthana, S. (2021). Targeting cryptic-orthosteric site of PD-L1 for
866 inhibitor identification using structure-guided approach. *Arch Biochem Biophys*, *713*, 109059.
867 https://doi.org/10.1016/j.abb.2021.109059
868 Mukhtasimova, N., Free, C., & Sine, S. M. (2005). Initial coupling of binding to gating mediated by
869 conserved residues in the muscle nicotinic receptor. *J Gen Physiol*, *126*(1), 23-39.
870 https://doi.org/10.1085/jgp.200509283
871 Munro, L., Ladefoged, L. K., Padmanathan, V., Andersen, S., Schiott, B., & Kristensen, A. S. (2019).
872 Conformational Changes in the 5-HT(3A) Receptor Extracellular Domain Measured by Voltage-
873 Clamp Fluorometry. *Molecular Pharmacology*, *96*(6), 720-734.
874 https://doi.org/10.1124/mol.119.116657
875 Muroi, Y., Theusch, C. M., Czajkowski, C., & Jackson, M. B. (2009). Distinct structural changes in the
876 GABAA receptor elicited by pentobarbital and GABA. *Biophys J*, *96*(2), 499-509.
877 https://doi.org/10.1016/j.bpj.2008.09.037
878 Nayak, T. K., & Auerbach, A. (2017). Cyclic activation of endplate acetylcholine receptors. *Proc Natl*
879 *Acad Sci U S A*, *114*(45), 11914-11919. https://doi.org/10.1073/pnas.1711228114
880 Nayak, T. K., Chakraborty, S., Zheng, W. J., & Auerbach, A. (2016). Structural correlates of affinity in
881 fetal versus adult endplate nicotinic receptors. *Nature Communications*, *7*.
882 https://doi.org/ARTN 11352
883 10.1038/ncomms11352
884 Nayak, T. K., Purohit, P. G., & Auerbach, A. (2012). The intrinsic energy of the gating isomerization of a
885 neuromuscular acetylcholine receptor channel. *J Gen Physiol*, *139*(5), 349-358.
886 https://doi.org/10.1085/jgp.201110752

887 Nayak, T. K., Vij, R., Bruhova, I., Shandilya, J., & Auerbach, A. (2019). Efficiency measures the
888 conversion of agonist binding energy into receptor conformational change. *J Gen Physiol*,
889 *151*(4), 465-477. https://doi.org/10.1085/jgp.201812215
890 Nickbarg, E. B., Davenport, R. C., Petsko, G. A., & Knowles, J. R. (1988). Triosephosphate isomerase:
891 removal of a putatively electrophilic histidine residue results in a subtle change in catalytic
892 mechanism. *Biochemistry*, *27*(16), 5948-5960. https://doi.org/10.1021/bi00416a019
893 Noviello, C. M., Gharpure, A., Mukhtasimova, N., Cabuco, R., Baxter, L., Borek, D., Sine, S. M., & Hibbs,
894 R. E. (2021). Structure and gating mechanism of the alpha7 nicotinic acetylcholine receptor.
895 *Cell*, *184*(8), 2121-2134 e2113. https://doi.org/10.1016/j.cell.2021.02.049
896 Padgett, C. L., Hanek, A. P., Lester, H. A., Dougherty, D. A., & Lummis, S. C. (2007). Unnatural amino
897 acid mutagenesis of the GABA(A) receptor binding site residues reveals a novel cation-pi
898 interaction between GABA and beta 2Tyr97. *Journal of Neuroscience*, *27*(4), 886-892.
899 https://doi.org/10.1523/JNEUROSCI.4791-06.2007
900 Pettersen, E. F., Goddard, T. D., Huang, C. C., Meng, E. C., Couch, G. S., Croll, T. I., Morris, J. H., & Ferrin,
901 T. E. (2021). UCSF ChimeraX: Structure visualization for researchers, educators, and developers.
902 *Protein Sci*, *30*(1), 70-82. https://doi.org/10.1002/pro.3943
903 Phillips, R. (2020). *The Molecular Switch: Signaling and Allostery*. Prinston University Press.
904 Plapp, B. V. (2010). Conformational changes and catalysis by alcohol dehydrogenase. *Arch Biochem*
905 *Biophys*, *493*(1), 3-12. https://doi.org/10.1016/j.abb.2009.07.001
906 Pless, S. A., Hanek, A. P., Price, K. L., Lynch, J. W., Lester, H. A., Dougherty, D. A., & Lummis, S. C. (2011).
907 A cation-pi interaction at a phenylalanine residue in the glycine receptor binding site is
908 conserved for different agonists. *Molecular Pharmacology*, *79*(4), 742-748.
909 https://doi.org/10.1124/mol.110.069583
910 Pless, S. A., & Lynch, J. W. (2009). Ligand-specific conformational changes in the alpha1 glycine
911 receptor ligand-binding domain. *J Biol Chem*, *284*(23), 15847-15856.
912 https://doi.org/10.1074/jbc.M809343200
913 Polovinkin, L., Hassaine, G., Perot, J., Neumann, E., Jensen, A. A., Lefebvre, S. N., Corringer, P. J.,
914 Neyton, J., Chipot, C., Dehez, F., Schoehn, G., & Nury, H. (2018). Conformational transitions of
915 the serotonin 5-HT(3) receptor. *Nature*, *563*(7730), 275-279. https://doi.org/10.1038/s41586-
916 018-0672-3
917 Purohit, P., & Auerbach, A. (2009). Unliganded gating of acetylcholine receptor channels. *Proc Natl*
918 *Acad Sci U S A*, *106*(1), 115-120. https://doi.org/10.1073/pnas.0809272106
919 Purohit, P., & Auerbach, A. (2013). Loop C and the mechanism of acetylcholine receptor-channel
920 gating. *J Gen Physiol*, *141*(4), 467-478. https://doi.org/10.1085/jgp.201210946
921 Purohit, P., Bruhova, I., Gupta, S., & Auerbach, A. (2014). Catch-and-Hold Activation of Muscle
922 Acetylcholine Receptors Having Transmitter Binding Site Mutations. *Biophysical Journal*, *107*(1),
923 88-99. https://doi.org/10.1016/j.bpj.2014.04.057
924 Purohit, P., Chakraborty, S., & Auerbach, A. (2015). Function of the M1 pi-helix in endplate receptor
925 activation and desensitization. *J Physiol*, *593*(13), 2851-2866. https://doi.org/10.1113/JP270223
926 Purohit, P., Gupta, S., Jadey, S., & Auerbach, A. (2013). Functional anatomy of an allosteric protein.
927 *Nature Communications*, *4*, 2984. https://doi.org/10.1038/ncomms3984
928 Purushotham, N., Singh, M., Paramesha, B., Kumar, V., Wakode, S., Banerjee, S. K., Poojary, B., &
929 Asthana, S. (2022). Design and synthesis of amino acid derivatives of substituted

930 benzimidazoles and pyrazoles as Sirt1 inhibitors. *RSC Adv*, *12*(7), 3809-3827.
931 https://doi.org/10.1039/d1ra06149f
932 Rahman, M. M., Basta, T., Teng, J., Lee, M., Worrell, B. T., Stowell, M. H. B., & Hibbs, R. E. (2022).
933 Structural mechanism of muscle nicotinic receptor desensitization and block by curare. *Nat*
934 *Struct Mol Biol*, *29*(4), 386-394. https://doi.org/10.1038/s41594-022-00737-3
935 Rahman, M. M., Teng, J., Worrell, B. T., Noviello, C. M., Lee, M., Karlin, A., Stowell, M. H. B., & Hibbs, R.
936 E. (2020). Structure of the Native Muscle-type Nicotinic Receptor and Inhibition by Snake
937 Venom Toxins. *Neuron*, *106*(6), 952-962 e955. https://doi.org/10.1016/j.neuron.2020.03.012
938 Rasmussen, S. G., DeVree, B. T., Zou, Y., Kruse, A. C., Chung, K. Y., Kobilka, T. S., Thian, F. S., Chae, P. S.,
939 Pardon, E., Calinski, D., Mathiesen, J. M., Shah, S. T., Lyons, J. A., Caffrey, M., Gellman, S. H.,
940 Steyaert, J., Skiniotis, G., Weis, W. I., Sunahara, R. K., & Kobilka, B. K. (2011). Crystal structure of
941 the beta2 adrenergic receptor-Gs protein complex. *Nature*, *477*(7366), 549-555.
942 https://doi.org/10.1038/nature10361
943 Rastelli, G., Del Rio, A., Degliesposti, G., & Sgobba, M. (2010). Fast and accurate predictions of binding
944 free energies using MM-PBSA and MM-GBSA. *J Comput Chem*, *31*(4), 797-810.
945 https://doi.org/10.1002/jcc.21372
946 Richard, J. P. (2022). Enabling Role of Ligand-Driven Conformational Changes in Enzyme Evolution.
947 *Biochemistry*, *61*(15), 1533-1542. https://doi.org/10.1021/acs.biochem.2c00178
948 Roe, D. R., & Cheatham, T. E., 3rd. (2013). PTRAJ and CPPTRAJ: Software for Processing and Analysis of
949 Molecular Dynamics Trajectory Data. *J Chem Theory Comput*, *9*(7), 3084-3095.
950 https://doi.org/10.1021/ct400341p
951 Sauguet, L., Shahsavar, A., Poitevin, F., Huon, C., Menny, A., Nemecz, A., Haouz, A., Changeux, J. P.,
952 Corringer, P. J., & Delarue, M. (2014). Crystal structures of a pentameric ligand-gated ion
953 channel provide a mechanism for activation. *Proc Natl Acad Sci U S A*, *111*(3), 966-971.
954 https://doi.org/10.1073/pnas.1314997111
955 Shang, Y., Yeatman, H. R., Provasi, D., Alt, A., Christopoulos, A., Canals, M., & Filizola, M. (2016).
956 Proposed Mode of Binding and Action of Positive Allosteric Modulators at Opioid Receptors.
957 *ACS Chem Biol*, *11*(5), 1220-1229. https://doi.org/10.1021/acschembio.5b00712
958 Sigel, E., & Steinmann, M. E. (2012). Structure, function, and modulation of GABA(A) receptors. *J Biol*
959 *Chem*, *287*(48), 40224-40231. https://doi.org/10.1074/jbc.R112.386664
960 Singh, M., Srivastava, M., Wakode, S. R., & Asthana, S. (2021). Elucidation of Structural Determinants
961 Delineates the Residues Playing Key Roles in Differential Dynamics and Selective Inhibition of
962 Sirt1-3. *Journal of Chemical Information and Modeling*, *61*(3), 1105-1124.
963 https://doi.org/10.1021/acs.jcim.0c01193
964 Srivastava, M., Mittal, L., Kumari, A., Agrahari, A. K., Singh, M., Mathur, R., & Asthana, S. (2022).
965 Characterizing (un)binding mechanism of USP7 inhibitors to unravel the cause of enhanced
966 binding potencies at allosteric checkpoint. *Protein Sci*, *31*(9), e4398.
967 https://doi.org/10.1002/pro.4398
968 Sun, H., Li, Y., Tian, S., Xu, L., & Hou, T. (2014). Assessing the performance of MM/PBSA and MM/GBSA
969 methods. 4. Accuracies of MM/PBSA and MM/GBSA methodologies evaluated by various
970 simulation protocols using PDBbind data set. *Phys Chem Chem Phys*, *16*(31), 16719-16729.
971 https://doi.org/10.1039/c4cp01388c

Taly, A., Corringer, P. J., Guedin, D., Lestage, P., & Changeux, J. P. (2009). Nicotinic receptors: allosteric transitions and therapeutic targets in the nervous system. *Nature Reviews Drug Discovery*, *8*(9), 733-750. https://doi.org/10.1038/nrd2927

Tarvin, R. D., Borghese, C. M., Sachs, W., Santos, J. C., Lu, Y., O'Connell, L. A., Cannatella, D. C., Harris, R. A., & Zakon, H. H. (2017). Interacting amino acid replacements allow poison frogs to evolve epibatidine resistance. *Science*, *357*(6357), 1261-1266. https://doi.org/10.1126/science.aan5061

Tian, C., Kasavajhala, K., Belfon, K. A. A., Raguette, L., Huang, H., Migues, A. N., Bickel, J., Wang, Y., Pincay, J., Wu, Q., & Simmerling, C. (2020). ff19SB: Amino-Acid-Specific Protein Backbone Parameters Trained against Quantum Mechanics Energy Surfaces in Solution. *J Chem Theory Comput*, *16*(1), 528-552. https://doi.org/10.1021/acs.jctc.9b00591

Tripathy, S., Zheng, W., & Auerbach, A. (2019). A single molecular distance predicts agonist binding energy in nicotinic receptors. *J Gen Physiol*, *151*(4), 452-464. https://doi.org/10.1085/jgp.201812212

Unwin, N. (1993). Nicotinic acetylcholine receptor at 9 A resolution. *J Mol Biol*, *229*(4), 1101-1124. https://doi.org/10.1006/jmbi.1993.1107

Vassetti, D., Pagliai, M., & Procacci, P. (2019). Assessment of GAFF2 and OPLS-AA General Force Fields in Combination with the Water Models TIP3P, SPCE, and OPC3 for the Solvation Free Energy of Druglike Organic Molecules. *J Chem Theory Comput*, *15*(3), 1983-1995. https://doi.org/10.1021/acs.jctc.8b01039

Vij, R., Purohit, P., & Auerbach, A. (2015). Modal affinities of endplate acetylcholine receptors caused by loop C mutations. *J Gen Physiol*, *146*(5), 375-386. https://doi.org/10.1085/jgp.201511503

Wagner, J. R., Sorensen, J., Hensley, N., Wong, C., Zhu, C., Perison, T., & Amaro, R. E. (2017). POVME 3.0: Software for Mapping Binding Pocket Flexibility. *J Chem Theory Comput*, *13*(9), 4584-4592. https://doi.org/10.1021/acs.jctc.7b00500

Walsh, R. M., Jr., Roh, S. H., Gharpure, A., Morales-Perez, C. L., Teng, J., & Hibbs, R. E. (2018). Structural principles of distinct assemblies of the human alpha4beta2 nicotinic receptor. *Nature*, *557*(7704), 261-265. https://doi.org/10.1038/s41586-018-0081-7

Wlodawer, A., & Erickson, J. W. (1993). Structure-based inhibitors of HIV-1 protease. *Annu Rev Biochem*, *62*, 543-585. https://doi.org/10.1146/annurev.bi.62.070193.002551

Xiu, X., Puskar, N. L., Shanata, J. A., Lester, H. A., & Dougherty, D. A. (2009). Nicotine binding to brain receptors requires a strong cation-pi interaction. *Nature*, *458*(7237), 534-537. https://doi.org/10.1038/nature07768

Yu, A., Salazar, H., Plested, A. J. R., & Lau, A. Y. (2018). Neurotransmitter Funneling Optimizes Glutamate Receptor Kinetics. *Neuron*, *97*(1), 139-149 e134. https://doi.org/10.1016/j.neuron.2017.11.024

Yu, R., Hurdiss, E., Greiner, T., Lape, R., Sivilotti, L., & Biggin, P. C. (2014). Agonist and antagonist binding in human glycine receptors. *Biochemistry*, *53*(38), 6041-6051. https://doi.org/10.1021/bi500815f

Zarkadas, E., Pebay-Peyroula, E., Thompson, M. J., Schoehn, G., Uchanski, T., Steyaert, J., Chipot, C., Dehez, F., Baenziger, J. E., & Nury, H. (2022). Conformational transitions and ligand-binding to a muscle-type nicotinic acetylcholine receptor. *Neuron*, *110*(8), 1358-1370 e1355. https://doi.org/10.1016/j.neuron.2022.01.013

1015 Zhong, W., Gallivan, J. P., Zhang, Y., Li, L., Lester, H. A., & Dougherty, D. A. (1998). From ab initio
1016 quantum mechanics to molecular neurobiology: a cation-pi binding site in the nicotinic
1017 receptor. *Proc Natl Acad Sci U S A*, *95*(21), 12088-12093.
1018 https://doi.org/10.1073/pnas.95.21.12088
1019